Application of first-order finite similitude in structural mechanics and earthquake engineering

DOI:
10.1002/eqe.3545

Document Version
Accepted author manuscript

APPLICATION OF FIRST-ORDER FINITE SIMILITUDE IN STRUCTURAL MECHANICS AND EARTHQUAKE ENGINEERING

Muhammed Atar, Keith Davey*, Rooholamin Darvizeh

School of Mechanical, Aerospace and Civil Engineering,

The University of Manchester, ManchesterM13 9PL, UK

ABSTRACT

An important experimental approach for the testing of earthquake-resistant structures is scaled experimentation with experimental designs impacted upon by the similitude theory of dimensional analysis. Unfortunately, the type of similitude provided by dimensional analysis seldom applies to complex structures, which is particularly problematic when scaling ratios are large. The issue is one of scale effects where the behaviour of the scaled version of any full-size structure can be markedly different.

Recently however a *new theory of scaling* called *finite similitude* has emerged in the open literature that confirms that the similitude offered by dimensional analysis is just one of a countable infinite number of alternative possibilities. The new theory of scaling raises the possibility that buildings and structures can be designed and tested in new ways and this aspect is the focus of this paper.

Similitude rules for single and two scaled experiments are examined to illustrate the benefits provided by alternative forms of similitude. The two types of similitude examined are termed *zeroth order* and *first order finite similitude*, which are shown to be two forms in an infinite number of alternative possibilities efficiently defined using a recursive relationship. The theory of scaling is founded on the metaphysical concept of space scaling yet provides the means to establish all scale dependencies for structural components and high-rise steel buildings along with buildings equipped with nonlinear-fluid viscous dampers for resisting earthquake loading conditions. It is shown through case-studies of increasing complexity how the new theory can be applied to reconstruct full-scale behaviours but also revealed are some of the limitations of the new approach.

KEYWORDS: finite similitude, scaled structures, dimensional analysis, time history analysis, scaled experimentation.

Corresponding author: keith.davey@manchester.ac.uk.

1. INTRODUCTION

Earthquake testing methods such as laboratory tests for massive structures such as tall bridges and skyscrapers commonly built today have become more challenging and less applicable. More feasible is the testing of scaled models to study the behaviour of such structures, as undoubtedly these forms of test are easier to perform and invariably are more cost effective to implement. Sized tests are especially recommended as one of the few experimental solutions for situations where it is impossible to test a real prototype. Although scaled experimentation has some significant limitations it still plays a critical role in process, product design and testing for systems. The obstacles to scaling are mainly related to the nonlinear relationships that exist between physical and scaled processes, which manifest as changes in physical behaviour with scale. Geometric scale dependencies are readily visible with geometric measures of length, area, and volume scaling linearly, quadratically and cubically, respectively. Important changes affected by changes in geometric measures in the structural analysis are surface forces and body forces with the latter decreasing at a faster rate than the former with scale. The presence of scale effects, which can be marked, has undoubtedly diminished the importance of scaled experimentation in recent times coupled with the ever-increasing sophistication of computational modelling, which has invariably accelerated this decline.

The issues surrounding scaling are generally well appreciated by the academic and industrial communities and it is appreciated that dimensional analysis provides the bedrock on which scaled experimentation is built, being fundamental to the concept of similarity. The prevailing view is that similar structures behave in the same way, and similarity can be investigated by applying dimensional analysis [1]. Similarity is rarely achievable for all but the simplest of structures and dimensional analysis provides no solution to dissimilar structures. In many respects, the concept of similarity, which is defined by dimensional analysis has not changed significantly for over a century and remains the dominant approach for academic and industrial scaled research. Linked to dimensional analysis is the Buckingham Pi theorem which reveals an inner dependence between dimensional variables [2] and more importantly brings into existence the dimensionless Pi groups. If it transpires that the Pi groups in the dimensionless equations governing the behaviour of the scaled and full-scale structures match, then the two structures are defined to be similar. However, as mentioned above, this situation is rarely met in reality [3] and the approach has shown little success in complex structures. Structural engineering has a long history of

investigations with scaled experimentation, but it is apparent on inspection of early historical references that most early forms of analysis were somewhat rudimentary in nature. The early work of Buckingham [2] provided the basis for more realistic scale models and the first significant application can be attributed to him [4], although the study was purely theoretical in scope. The ground-breaking work of Buckingham [2] was followed by an almost exponential rise in the numbers of publications investigating the application of scaled methods.

In a general sense, scaled experimentation is principally about the establishment of scaling rules, which provides a means to transfer obtained pieces of information from the scaled experiment to the full scale. The focus here is on earthquake seismic tests but it is recognized that there exist limitations with scaling. Practical limitations might be the unavailability of materials with the required material properties but also the availability of suitable experimental equipment can place constraints on what is possible. In the case of seismic testing a critically important and often utilized piece of apparatus is a shake table. Well-researched scaling rules are often imposed in the application of shake-table studies, as achieving complete similarity is unlikely. Many scaled experiments have been performed and publications produced addressing this issue to better understand the behaviour of structures under earthquake excitations. Sharma et al. [5], Nayak et al. [6], Guerrero et al. [7], and Garevski et al. [8], studied the behaviour of scaled-down structures in order to predict the behaviour of physical models by applying several similarity laws. The benefits and limitations of using different materials in small-scaled models were investigated in reference [10]. Other studies include investigations into aspects of inelastic behaviour of structures [9] and unreinforced structures such as masonry at half scale [10]. Research using relatively high scaling factors included the application of two-dimensional base ground motion, which induces complex behaviour for a high-rise tall building [11] at a 1/50 scale. Another example at 1/40 scale is the scaling of high-rise buildings studied to investigate the behaviour of huge structures [12] [13].

The difficulty with all the scaled experimental studies mentioned above is that they are all constrained by the limited capability of dimensional analysis with the prevalence of scale effects as presently defined. A particular example is related to weight and body forces and the associated requirement in scaling for mass to be added to the scaled model [14]. Typically, masses are added in the form of blocks attached to slabs but fixing one problem invariably produces another as it can be anticipated that the behaviour of the supporting frame will not be correct during collapse. The blocks of mass can move and even collide under deformation conditions and the result can be unrepresentative behaviour. Additional mass is often essential when scaling down dimensions whilst maintaining the material properties of the prototype. The added mass however comes with drawbacks as it makes movement and control invariably more complex [15][16]. Simulator control becomes more difficult since additional mass has the potential to produce overturning moments. This often means that specimens have to be designed using bigger scaling factors and involve control measures so that the above drawbacks can to a certain degree be accommodated depending on the payload capacities of the shake table utilized [15]. Investigated in reference [17] is a rotational system involving restraining cables to limit the extent of translation of rotational mass. The device was designed to allow mass movement up to a maximum displacement limit at which point the restraining cables stopped further movement; the cessation of mass movement was termed specimen failure. Unfortunately however, the scaled system cannot be said to be truly representative and in particular the loading and overall stiffness of the scaled model was influenced [17]. Another study [18] concerned with the seismic performance of a tall bridge using a shake table test also required additional mass. The precise distribution of the mass could be through the pier height determined by means of repeated numerical trials to finalize the location of the masses. It is evident that additional mass comes with problems and an alternative option is to increase the acceleration according to similarity laws. Unfortunately, this solution comes with its own shortcoming since for representative behaviours of high-rise buildings it is needed to apply large accelerations. This is practically difficult to arrange due to the limits of laboratory shake table capacities.

It is clear from the evidence of past experimental studies that the limitations imposed by the current definition of similarity has led to all manner of contortions to address the unrepresentative behaviour of scaled models. The present situation is not satisfactory, and the solutions investigated involving additional mass, makeshift scaling rules, artificially high accelerations are not fit for purpose. To address this problem this paper examines two alternative forms of similitude that form part of a new *scaling theory* termed *finite similitude* [19–24]. The work here is designed to provide additional evidence on the merit of the newer forms of similarity and add to earlier works done in the fields of: metal forming [21], impact mechanics [23], powder compaction [19], and biomechanics [22]. These studies were limited to one scaled experiment under the similitude rule named *zeroth-order finite similitude*. Both zeroth-order finite similitude and dimensional analysis are underpinned by proportional field relationships, assumed *a priori* for dimensional analysis, and returned *a posteriori* from the invariance principle applied to define zeroth-order finite similitude. Consequently, it is possible for each of the approaches to replicate each of the others similitude conditions. Despite this association however, zeroth-order finite similitude has the advantage of being part of a holistic scaling theory with scaling identities and the number of freedoms identified, which provides a route for direct optimization (see references [21,23] for greater details). Dimensional analysis on the other hand is well known, links fully to approximate physics with the retention of dominant dimensionless terms, and benefits from its association with the Buckingham Pi theorem for reducing

the number of arguments in a dimensioned expression. The work presented here is concerned with both zeroth order and first-order similitude, so involves both one and two-scaled experiments although focusing on seismic studies. The proposed two-experiment approach to scaled experimentation first appeared in references [25,26] for the study of impact mechanics and discrete dynamic systems. The work here extends the application of the method to seismic systems involving steel buildings and non-linear damping, and for the first time the breaking of geometric similarity in structural members.

The starting point for the finite similitude theory is rather unusual in that it begins with a concept that cannot be physically enacted, which is space scaling. The concept is introduced in Sec. 2, where it is shown how metaphysical-space scaling provides the correct founding theory for the *theory of scaling* providing an intuitive vision for scaling. The mathematics of space scaling is relatively straightforward and ultimately provides the means to examine scaled structural mechanics. This achieved in a roundabout way however, which first requires describing the impact of space scaling on control volumes as these underpin mechanics in its transport form. The key step in the finite similitude theory presented in Sec. 2 is the projection of transport equations defined on the trial space (where the scaled experiment resides) onto the physical space (where the full-scale structure resides). This projection reveals in one form or another all the scale dependencies possible in structural mechanics. The approach effectively transforms the problem of scaling into one whose objective is the revealing of those fields that are only defined implicitly by the projection between trial and physical space. This can be achieved with the application of similitude rules and unlike dimensional analysis the finite similitude approach is not limited to a single similitude condition. Alternative rules of similitude are presented in Sec. 3, where a countable infinite number of similitude identities are defined under what is termed high-order finite similitude. The rules provide a calculus for scaling in that they describe how scaled systems change with scale. Integration of the differential equations defined by high-order finite similitude links experiments at distinct scales. The two integrated forms of interest in this paper presented in Sec. 3 are termed zeroth order and first order finite similitude and involve one and two scaled experiments, respectively. To demonstrate the practical advantage of the new scaling theory in structural mechanics the behaviour of important structural elements is examined under the new rules of scaling. Considered in Sec. 4 are a beam-strut model exposed to a point load, a column buckling analysis and a thin-section problem, which breaks the rule of geometric similarity by allowing thickness to be constrained. A more complicated structure is considered in Sec. 5, where the first-order finite similitude rule is applied to a high-rise steel building exposed to a real earthquake load. Further complication is added in Sec. 6, where an eight-story steel construction equipped with nonlinear fluid viscous dampers is examined under scaling and subject to earthquake excitation. Through standard structural elements to building designs with and without nonlinear dampers the paper aims to demonstrate the benefits and validity of the new scaling theory. The paper ends with a brief set of conclusions confirming that the downside of additional scaled experiments is counterbalanced by the benefits of increased flexibility and accuracy.

2. THE THEORY OF SCALING: A REVIEW OF FINITE SIMILITUDE

The difficulty with all past studies into scaled experimentation is the absence of a scaling theory that can account for all scale dependencies that arise. The finite-similitude theory accounts for scaled dependencies by means of a metaphysical concept of space scaling. Although it is evidently impossible to scale space the concept can nevertheless be defined mathematically by introducing a map between the space which houses the full-scale experiment (the physical space) and the space where the scaled experiment resides (the trial space). In mathematical terms the temporally invariant map between coordinate functions in the physical and trial space take the form $x_{ps} \mapsto x_{ts}$, where the subscripts "ps" and "ts" signify physical and trial space, respectively. In differential terms and limiting the space scaling to isotropic scaling the map takes the form $d\boldsymbol{x}_{ts} = \beta d\boldsymbol{x}_{ps}$, which in coefficient terms gives $dx^i_{ts} = \beta dx^i_{ps}$. It is assumed here that coordinate system in each space is orthonormal and under this restriction positive scalar β indicates the extent of linear isotropic scaling with $0 < \beta < 1$ for contraction, $\beta = 1$ for no scaling and $\beta > 1$ for expansion. Although space contraction is of particular interest with scaled-down experiments the theory does allow scaling up also. As Newtonian physics is the focus of the study absolute times t_{ps} and t_{ts} are assumed to exist with each space possessing a single measure of time. It is also necessary to establish a relationship between t_{ps} and t_{ts}, which in differential terms takes the form $dt_{ts} = g dt_{ps}$ for positive scalar g [25].

2.1. Control Volume Motion

To relate the effect space scaling has on the governing physics it is necessary to have the physics described by an appropriate formulation. The correct approach is one based on a control-volume formulation as control volumes are basically regions of space and hence are immediately impacted upon by space scaling. Although in some respects this approach might appear remote from structural engineering it is nevertheless necessary and is simply

the path followed by the theory from space to control volumes (regions of space) to transport equations (laws of nature) and finally to structural field relationships.

The mathematics of control volume motion which can be found in reference [27–29] and involves transport of a control volume Ω_{ts}^{*} (in the trial space) by means of a velocity field $\boldsymbol{v}_{ts}^{*}$. To define the motion of anything it is generally with respect to something else, and by comparing Ω_{ts}^{*} with a reference control volume Ω_{ts}^{*ref} it is possible to define the following partial derivative,

$$\boldsymbol{v}_{ts}^{*}=\frac{D^{*}\boldsymbol{x}_{ts}^{*}}{D^{*}t_{ts}}=\left.\frac{\partial \boldsymbol{x}_{ts}^{*}}{\partial t_{ts}}\right|_{\boldsymbol{\chi}_{ts}} \tag{1}$$

where coordinate points $\boldsymbol{\chi}_{ts}\in\Omega_{ts}^{*ref}$ and $\boldsymbol{x}_{ts}\in\Omega_{ts}^{*}$, and $\frac{D^{*}}{D^{*}t_{ts}}$ represents a partial temporal derivative where the reference point $\boldsymbol{\chi}_{ts}$ is held constant.

The exact same apparatus can be utilized in the physical space but motion of the two control volumes must be related in some manner. Note that as shown in reference [25] there exists a map between two control volumes in physical and trial spaces such that $d\boldsymbol{x}_{ts}^{*}=\beta d\boldsymbol{x}_{ps}^{*}$, i.e., essentially that provided by the space scaling map. The maps $d\boldsymbol{x}_{ts}^{*}=\beta d\boldsymbol{x}_{ps}^{*}$ and $dt_{ts}=gdt_{ps}$ immediately provide a similitude velocity relationship $\boldsymbol{v}_{ts}^{*}=g^{-1}\beta\boldsymbol{v}_{ps}^{*}$ which is a relatively simple expression relating the velocities of the moving control volumes in the two spaces. With the synchronization of the moving control volumes established it is now possible to examine the governing equations for structural mechanics in transport form.

2.2. Transport Form of Projected Structural Mechanics

The key step in the finite-similitude theory is the projection of the governing transport equations for the trial space onto the physical space because it is through this operation that scale dependencies are exposed. For structural analysis, the four transport equations (essentially eight as two are vector equations) of interest are those for volume, continuity, momentum and movement. The related transport equations can be written in the form:

$$\frac{D^{*}}{D^{*}t_{ts}}\int_{\Omega_{ts}^{*}}dV_{ts}^{*}-\int_{\Gamma_{ts}^{*}}\boldsymbol{v}_{ts}^{*}\cdot\boldsymbol{n}_{ts}d\Gamma_{ts}^{*}=0 \tag{2a}$$

$$\frac{D^{*}}{D^{*}t_{ts}}\int_{\Omega_{ts}^{*}}\rho_{ts}dV_{ts}^{*}+\int_{\Gamma_{ts}^{*}}\rho_{ts}\left(\boldsymbol{v}_{ts}-\boldsymbol{v}_{ts}^{*}\right)\cdot\boldsymbol{n}_{ts}d\Gamma_{ts}^{*}=0 \tag{2b}$$

$$\frac{D^{*}}{D^{*}t_{ts}}\int_{\Omega_{ts}^{*}}\rho_{ts}\boldsymbol{v}_{ts}dV_{ts}^{*}+\int_{\Gamma_{ts}^{*}}\rho_{ts}\boldsymbol{v}_{ts}\left(\boldsymbol{v}_{ts}-\boldsymbol{v}_{ts}^{*}\right)\cdot\boldsymbol{n}_{ts}d\Gamma_{ts}^{*}-\int_{\Gamma_{ts}^{*}}\boldsymbol{\sigma}_{ts}\cdot\boldsymbol{n}_{ts}d\Gamma_{ts}^{*}-\int_{\Omega_{ts}^{*}}\rho_{ts}\boldsymbol{b}_{ts}dV_{ts}^{*}=0 \tag{2c}$$

$$\frac{D^{*}}{D^{*}t_{ts}}\int_{\Omega_{ts}^{*}}\rho_{ts}\boldsymbol{u}_{ts}dV_{ts}^{*}+\int_{\Gamma_{ts}^{*}}\rho_{ts}\boldsymbol{u}_{ts}\left(\boldsymbol{v}_{ts}-\boldsymbol{v}_{ts}^{*}\right)\cdot\boldsymbol{n}_{ts}d\Gamma_{ts}^{*}-\int_{\Omega_{ts}^{*}}\rho_{ts}\boldsymbol{v}_{ts}dV_{ts}^{*}=0 \tag{2d}$$

where ρ_{ts} is mass density, $\boldsymbol{v}_{ts}$ is material velocity, $\boldsymbol{u}_{ts}$ is material displacement, $\boldsymbol{\sigma}_{ts}$ is Cauchy stress and $\boldsymbol{b}_{ts}$ is specific-body force (i.e. force per unit mass) for the trial space.

These equations are sufficient for physical modelling in structural engineering, with Eq. (2a) enforcing control volume synchronization, Eq. (2b) allowing for density to change, Eq. (2c) being the all-important momentum equation, and Eq. (2d) first introduced in reference [30] providing a description for displacement $\boldsymbol{u}_{ts}$. With the governing constraining equations defined the next step in the finite similitude theory is the most critical as it quantifies either explicitly or implicitly all scale dependencies. This quantification is achieved by projecting the transport equations in the trial space (i.e., Eqs. (2)) onto the physical space. The projection is made possible by the existence of the map between the control volumes in the physical and trial space. Thus the relationship $d\boldsymbol{x}_{ts}^{*}=\beta d\boldsymbol{x}_{ps}^{*}$ provides the expressions $dV_{ts}^{*}=\beta^{3}dV_{ps}^{*}$ and $\boldsymbol{n}_{ts}d\Gamma_{ts}^{*}=\beta^{2}\boldsymbol{n}_{ps}d\Gamma_{ps}^{*}$, and recalling the time relationship $dt_{ts}=gdt_{ps}$, it is possible to substitute these into Eqs. (3). In addition to multiplication of Eqs. (2) by g each equation is individually multiplied by the scaling parameters α_{0}^{1}, α_{0}^{ρ}, α_{0}^{v} and α_{0}^{u} (the role of these is explained below) to provide

$$\alpha_{0}^{1}T_{0}^{1}\left(\beta\right)=\frac{D^{*}}{D^{*}t_{ps}}\int_{\Omega_{ps}^{*}}\alpha_{0}^{1}\beta^{3}dV_{ps}^{*}-\int_{\Gamma_{ps}^{*}}\alpha_{0}^{1}\beta^{3}\boldsymbol{v}_{ps}^{*}\cdot\boldsymbol{n}_{ps}d\Gamma_{ps}^{*}=0 \tag{3a}$$

$$\alpha_0^{\rho}T_0^{\rho}(\beta)=\frac{D^*}{D^*t_{ps}}\int_{\Omega_{ps}^*}\alpha_0^{\rho}\beta^3\rho_{ts}dV_{ps}^*+\int_{\Gamma_{ps}^*}\alpha_0^{\rho}\beta^3\rho_{ts}\left(\boldsymbol{V}_{ps}-\boldsymbol{v}_{ps}^*\right)\cdot\boldsymbol{n}_{ps}d\Gamma_{ps}^*=0 \tag{3b}$$

$$\alpha_0^{v}T_0^{v}(\beta)=\frac{D^*}{D^*t_{ps}}\int_{\Omega_{ps}^*}\left(\alpha_0^{v}g^{-1}\beta\right)\beta^3\rho_{ts}\boldsymbol{V}_{ps}dV_{ts}^*+\int_{\Gamma_{ps}^*}\left(\alpha_0^{v}g^{-1}\beta\right)\beta^3\rho_{ts}\boldsymbol{V}_{ps}\left(\boldsymbol{V}_{ts}-\boldsymbol{v}_{ps}^*\right)\cdot\boldsymbol{n}_{ps}d\Gamma_{ps}^*$$
$$-\int_{\Gamma_{ps}^*}\boldsymbol{\Sigma}_{ps}\cdot\boldsymbol{n}_{ps}d\Gamma_{ps}^*-\int_{\Omega_{ps}^*}\boldsymbol{B}_{ps}dV_{ps}^*=0 \tag{3c}$$

$$\alpha_0^{u}T_0^{u}(\beta)=\frac{D^*}{D^*t_{ps}}\int_{\Omega_{ps}^*}\left(\alpha_0^{u}\beta\right)\beta^3\rho_{ts}\boldsymbol{U}_{ts}dV_{ps}^*+\int_{\Gamma_{ts}^*}\left(\alpha_0^{u}\beta\right)\beta^3\rho_{ts}\boldsymbol{U}_{ps}\left(\boldsymbol{V}_{ps}-\boldsymbol{v}_{ps}^*\right)\cdot\boldsymbol{n}_{ps}d\Gamma_{ps}^*$$
$$-\int_{\Omega_{ps}^*}\left(\alpha_0^{u}\beta\right)\beta^3\rho_{ts}\boldsymbol{V}_{ps}dV_{ps}^*=0 \tag{3d}$$

where $\boldsymbol{V}_{ps}=\beta^{-1}g\boldsymbol{v}_{ts}$, $\boldsymbol{U}_{ps}=\beta^{-1}\boldsymbol{u}_{ts}$, $\boldsymbol{\Sigma}_{ps}=\alpha_0^{v}g\beta^2\boldsymbol{\sigma}_{ts}$ and $\boldsymbol{B}_{ps}=\alpha_0^{v}g\beta^3\rho_{ts}\boldsymbol{b}_{ts}$

Although somewhat complicated looking, Eqs. (3) are no more than Eqs. (2) but played out on the physical space; no approximation is involved in this projection. The importance of Eqs. (3) is that they reveal all scale dependencies in one form or another. Some of the scale dependencies are explicit and recognizable, such as β^3 and β^2 which arise from changes in the geometric measures of volume and area, yet others are implicit, i.e. tensor field $\boldsymbol{\Sigma}_{ps}(\beta)$, vector fields $\boldsymbol{V}_{ps}(\beta)$, $\boldsymbol{U}_{ps}(\beta)$, and $\boldsymbol{B}_{ps}(\beta)$, and scalar field $\rho_{ts}(\beta)$. The dependence of these fields on β is a consequence of the fact that the trial space is at a particular β and changing this influences the fields in that space and likewise those projected onto the physical space. The problem of scaling has been transformed into a problem where the objective is to make explicit those fields that are an implicit function of β. Once this is achieved then scaling is solved since it is then possible to know what happens at full scale from a scaled experiment. To reveal the field dependencies there are two main approaches, with the first approach requiring more information (e.g., size and surface effects) about the specific problem under consideration. A more generic approach is to assume that the physical behaviours follow a particular similitude rule. Similitude rules provide the means to design experiments and a particular advantage offered by Eqs. (3) is that unlike dimensional analysis, alternative similitude rules can be explored. The downside is that similitude rules are invariably restrictive and consequently there is no guaranteed that an experimental arrangement will fall within the solution space provided by a particular rule. However, with physical modelling and the use of alternative materials the solution space offered by a similitude rule can be enlarged but this invariably requires the existence of substitute materials with the necessary peculiar properties.

3. SIMILITUDE RULES

The focus of this section is on the definition of similitude with the objective to reveal the behaviours of the hidden fields in Eqs. (3). The main transport equations can be succinctly represented in the form $\alpha_0^{\psi}T_0^{\psi}=0$, where ψ can be set to 1, ρ, v and u. The first and possibly an obvious similitude assumption is that $\alpha_0^{\psi}T_0^{\psi}(\beta)$ does not change with β, which in mathematically terms is the identity,

$$\frac{d}{d\beta}\left(\alpha_0^{\psi}T_0^{\psi}\right)\equiv 0 \tag{4}$$

where the symbol "$\equiv$" signifies identically zero, which means the left-hand side of this equation vanishes completely under the derivative.

The identity is equivalent to what is provided by dimensional analysis since integration between the limits β and $\beta=1$ provides $\alpha_0^{\psi}T_0^{\psi}(\beta)\equiv\alpha_0^{\psi}T_0^{\psi}(1)=T_{0ps}^{\psi}$, with the necessity that $\alpha_0^{\psi}(1)=1$, required so that projected transport equations at $\beta=1$ match $T_{0ps}^{\psi}=0$. The identity $\alpha_0^{\psi}T_0^{\psi}(\beta)\equiv T_{0ps}^{\psi}$ provides an invariance between the projected trial-space equations (and by implication the original trial-space equations), with the physical space transport equations. Note the role played by $\alpha_0^{\psi}(\beta)$ in facilitating the application of a single identity (i.e., Eq. (4)) to all the transport equations, which can be likened to the role played by making equations dimensionless in dimensional analysis. Detailed studies on the application of Eq. (4) (termed zeroth order finite similitude) can be found in references [19–21,23,24], where specific zeroth-order relationships relating to density, velocity, displacement etc. can be found. The advantage offered by Eqs. (3) is that unlike dimensional analysis the approach is not limited to a single similitude identity and a countable infinite number of identities can be readily defined as follows:

3.1. Definition (High-order finite similitude)

The similitude rule for k^{th}-order finite similitude is identified by the lowest derivative that satisfies:

$$T_{k+1}^{\psi} = \frac{d}{d\beta}\left(\alpha_k^{\psi} T_k^{\psi}\right) \equiv 0 \tag{5}$$

for all $\beta > 0$ with $\alpha_0^{\psi} T_0^{\psi}$ defined by Eqs. (3) and the scalars α_k^{ψ} being a function of β with $\alpha_k^{\psi}(1) = 1$.

Note the contention here that similarity is no more than imposed rules that provide a convenient means to reveal hidden field relationships and that for the past century only one rule has been assumed to exist. However, despite Eq. (5) being a mere definition, it possesses certain attributes that make it highly suited to similarity. Firstly, lower-order forms of similitude are contained in higher-order forms; for example, zeroth order ($T_1^{\psi} \equiv 0$) automatically satisfies first order ($T_2^{\psi} = \frac{d}{d\beta}\left(\alpha_1^{\psi} T_1^{\psi}\right) \equiv 0$), and any higher order (easily shown by induction), which is a desirable if not necessary feature. All the scaling functions α_k^{ψ} play identical roles, i.e., the annihilation of β in the equations $\alpha_k^{\psi} T_k^{\psi} = 0$ to satisfy the similitude rule Eq. (6). The equations $\alpha_k^{\psi} T_k^{\psi} = 0$ are in the form of transport equations whose fields are derivatives (with respect to β) of those fields that appear in Eqs. (3) (i.e., in $\alpha_0^{\psi} T_0^{\psi} = 0$); this aspect is not explored further here. Shown below is how Eq. (5) can be integrated on forming a divided-difference table, which enables discrete identities to be formed with relative ease for application to scaled experimentation. It transpires that Eq. (5) leads to physically intuitive proportionality relationships for certain fields, field differences, field differences of differences and so on. Each increment in order requires an additional scaled experiment with zeroth order requiring only one scaled experiment, first order requiring two and so on. The reason for this is related to the order of the highest derivative in the similitude rule and for example substitution for $T_1^{\psi} = \frac{d}{d\beta}\left(\alpha_0^{\psi} T_0^{\psi}\right)$ into the identity $T_2^{\psi} = \frac{d}{d\beta}\left(\alpha_1^{\psi} T_1^{\psi}\right) \equiv 0$ provides,

$$T_2^{\psi} = \frac{d}{d\beta}\left(\alpha_1^{\psi} T_1^{\psi}\right) = \frac{d}{d\beta}\left(\alpha_1^{\psi} \frac{d}{d\beta}\left(\alpha_0^{\psi} T_0^{\psi}\right)\right) \equiv 0 \tag{6a}$$

which is the similitude rule for first-order finite similitude and was first introduced in reference [25].

The two derivatives present in Eq. (6a) indicate that on integration, two scaled experiments are involved with a similitude rule that connects these to the full-scale system. The next level up is second order, which takes the form,

$$T_3^{\psi} = \frac{d}{d\beta}\left(\alpha_2^{\psi} T_2^{\psi}\right) = \frac{d}{d\beta}\left(\alpha_2^{\psi} \frac{d}{d\beta}\left(\alpha_1^{\psi} T_1^{\psi}\right)\right) = \frac{d}{d\beta}\left(\alpha_2^{\psi} \frac{d}{d\beta}\left(\alpha_1^{\psi} \frac{d}{d\beta}\left(\alpha_0^{\psi} T_0^{\psi}\right)\right)\right) \equiv 0 \tag{6b}$$

and the presence of three nested derivatives indicates the need for three scaled experiments.

3.2. First-order Solutions

The prime interest in this paper is on the application of first-order finite similitude to non-trivial practical structural-engineering problems. Prior to examining the first order rules it is necessary to substitute into Eqs. (3) pertinent zeroth-order conditions obtained from identity Eq. (4), which are $\rho_{ps} = \alpha_0^{\rho} \beta^3 \rho_{ts}$, $\alpha_0^1 = \beta^{-3}$, $\alpha_0^v = g\beta^{-1}\alpha_0^{\rho}$ and $\alpha_0^u = \beta^{-1}\alpha_0^{\rho}$ to provide

$$\alpha_0^{\rho} T_0^{\rho}(\beta) = \frac{D^*}{D^* t_{ps}} \int_{\Omega_{ps}^*} \rho_{ps} dV_{ps}^* + \int_{\Gamma_{ps}^*} \rho_{ps}\left(\boldsymbol{V}_{ps} - \boldsymbol{v}_{ps}^*\right) \cdot \boldsymbol{n}_{ps} d\Gamma_{ps}^* = 0 \tag{7a}$$

$$\alpha_0^{v} T_0^{v}(\beta) = \frac{D^*}{D^* t_{ps}} \int_{\Omega_{ps}^*} \rho_{ps} \boldsymbol{V}_{ps} dV_{ts}^* + \int_{\Gamma_{ps}^*} \rho_{ps} \boldsymbol{V}_{ps}\left(\boldsymbol{v}_{ts} - \boldsymbol{v}_{ps}^*\right) \cdot \boldsymbol{n}_{ps} d\Gamma_{ps}^* - \int_{\Gamma_{ps}^*} \boldsymbol{\Sigma}_{ts} \cdot \boldsymbol{n}_{ps} d\Gamma_{ps}^* - \int_{\Omega_{ps}^*} \boldsymbol{B}_{ts} dV_{ps}^* = 0 \tag{7b}$$

$$\alpha_0^{u} T_0^{u}(\beta) = \frac{D^*}{D^* t_{ps}} \int_{\Omega_{ps}^*} \rho_{ps} \boldsymbol{U}_{ts} dV_{ps}^* + \int_{\Gamma_{ps}^*} \rho_{ps} \boldsymbol{U}_{ps}\left(\boldsymbol{v}_{ps} - \boldsymbol{v}_{ps}^*\right) \cdot \boldsymbol{n}_{ps} d\Gamma_{ps}^* - \int_{\Omega_{ps}^*} \rho_{ps} \boldsymbol{V}_{ps} dV_{ps}^* = 0 \tag{7c}$$

where $\boldsymbol{\Sigma}_{ps} = \alpha_0^{v} g \beta^2 \boldsymbol{\sigma}_{ts}$, $\boldsymbol{B}_{ts} = \alpha_0^{v} g \beta^3 \rho_{ts} \boldsymbol{b}_{ts} = g^2 \beta^{-1} \boldsymbol{b}_{ts}$, and where it is recognized that the condition $\alpha_0^1 = \beta^{-3}$ ensures that Eq. (3a) satisfies Eq. (4) (and consequently Eq. (6a)), so is of no further concern.

To avoid the necessity for second-order finite similitude the term $\boldsymbol{V}_{ts} - \boldsymbol{v}^{*}_{ps}$ is replaced by the zeroth-order approximation $\boldsymbol{v}_{ts} - \boldsymbol{v}^{*}_{ps}$ in the movement and momentum equations to reflect the fact that convective-type terms are of little concern in structural engineering. The transformation of Eqs. (6) into the required discrete integrated form can be readily achieved by means of a divided-difference table (see Table 1) and observe that the focus on behaviour at $\beta_0 = 1$ and down scaling means backward differences are required. In addition, unlike a traditional divided-difference table a mean-value theorem is applied to ensure exact differences are returned. In particular, the first divided differences in column three in Table 1 are obtained from the identities,

Table 1: Divided difference table for first-order theory

β_i	$\alpha_0^{\psi}\mathbf{T}_0^{\psi}\left(\beta_i\right)$	First Divided Difference	Second Divided Difference
β_2	$\alpha_0^{\psi}\mathbf{T}_0^{\psi}\left(\beta_2\right)$		
		$\alpha_1^{\psi}\mathbf{T}_1^{\psi}\left(\beta_2^1\right)$	
β_1	$\alpha_0^{\psi}\mathbf{T}_0^{\psi}\left(\beta_1\right)$		$\dfrac{\alpha_1^{\psi}\mathbf{T}_1^{\psi}\left(\beta_1^0\right) - \alpha_1^{\psi}\mathbf{T}_1^{\psi}\left(\beta_2^1\right)}{\beta_1^0 - \beta_2^1} \equiv 0$
		$\alpha_1^{\psi}\mathbf{T}_1^{\psi}\left(\beta_1^0\right)$	
β_0	$\alpha_0^{\psi}\mathbf{T}_0^{\psi}\left(\beta_0\right)$		

$$\alpha_1^{\psi}\mathbf{T}_1^{\psi}\left(\beta_2^1\right) \equiv \alpha_1^{\psi}\left(\beta_2^1\right)\frac{\alpha_0^{\psi}\mathbf{T}_0^{\psi}\left(\beta_1\right) - \alpha_0^{\psi}\mathbf{T}_0^{\psi}\left(\beta_2\right)}{\beta_1 - \beta_2} \tag{8a}$$

$$\alpha_1^{\psi}\mathbf{T}_1^{\psi}\left(\beta_1^0\right) \equiv \alpha_1^{\psi}\left(\beta_1^0\right)\frac{\alpha_0^{\psi}\mathbf{T}_0^{\psi}\left(\beta_0\right) - \alpha_0^{\psi}\mathbf{T}_0^{\psi}\left(\beta_1\right)}{\beta_0 - \beta_1} \tag{8b}$$

where $\beta_2 \le \beta_2^1 \le \beta_1$ and $\beta_1 \le \beta_1^0 \le \beta_0$ on application of a mean-value theorem, and where β_2 and β_1 are distinct scales such that $\beta_2 < \beta_1 < \beta_0 = 1$.

The second divided difference in column four in Table 1 is identically zero as is evident on integration of Eq. (6a) between the limits β_2^1 and β_1^0. It follows then on substitution of Eqs. (8) into the identity $\alpha_1^{\psi}T_1^{\psi}\left(\beta_1^0\right) \equiv \alpha_1^{\psi}T_1^{\psi}\left(\beta_2^1\right)$, and following some reorganization, that the required discrete sought identity

$$\alpha_0^{\psi}\mathbf{T}_0^{\psi}\left(\beta_0\right) \equiv \alpha_0^{\psi}\mathbf{T}_0^{\psi}\left(\beta_1\right) + R_1^{\psi}\left(\alpha_0^{\psi}\mathbf{T}_0^{\psi}\left(\beta_1\right) - \alpha_0^{\psi}\mathbf{T}_0^{\psi}\left(\beta_2\right)\right) \tag{9}$$

is obtained where,

$$R_1^{\psi} = \left(\frac{\alpha_1^{\psi}\left(\beta_2^1\right)}{\alpha_1^{\psi}\left(\beta_1^0\right)}\right)\left(\frac{\beta_0 - \beta_1}{\beta_1 - \beta_2}\right) \tag{10}$$

and where R_1^{ψ} takes the form of a parameter arising for the indeterminacy of the function $\alpha_1^{\psi}\left(\beta\right)$.

Note that Eq. (9) provides transport equations for the physical space formed from information at the two scales β_2 and β_1. It is by this means that equations constraining the behaviour at the two scales β_2 and β_1 also constrain the behaviour at the full scale β_0. Application of Eq. (9) to the governing transport equations (i.e., Eqs. (7)), return the all-important first-order field identities

$$\boldsymbol{v}_{ps} = \boldsymbol{V}_{ps}\left(\beta_1\right) + R_1^{\rho}\left(\boldsymbol{V}_{ps}\left(\beta_1\right) - \boldsymbol{V}_{ps}\left(\beta_2\right)\right) \tag{11a}$$

$$\boldsymbol{v}_{ps} = \boldsymbol{V}_{ps}\left(\beta_1\right) + R_1^{v}\left(\boldsymbol{V}_{ps}\left(\beta_1\right) - \boldsymbol{V}_{ps}\left(\beta_2\right)\right) \tag{11b}$$

$$\boldsymbol{\sigma}_{ps} = \boldsymbol{\Sigma}_{ps}\left(\beta_1\right) + R_1^{v}\left(\boldsymbol{\Sigma}_{ps}\left(\beta_1\right) - \boldsymbol{\Sigma}_{ps}\left(\beta_2\right)\right) \tag{11c}$$

$$\boldsymbol{b}_{ps} = \boldsymbol{B}_{ps}\left(\beta_1\right) + R_1^{v}\left(\boldsymbol{B}_{ps}\left(\beta_1\right) - \boldsymbol{B}_{ps}\left(\beta_2\right)\right) \tag{11d}$$

$$\boldsymbol{u}_{ps} = \boldsymbol{U}_{ps}\left(\beta_1\right) + R_1^{u}\left(\boldsymbol{U}_{ps}\left(\beta_1\right) - \boldsymbol{U}_{ps}\left(\beta_2\right)\right) \tag{11e}$$

$$\boldsymbol{v}_{ps} = \boldsymbol{V}_{ps}\left(\beta_1\right) + R_1^{u}\left(\boldsymbol{V}_{ps}\left(\beta_1\right) - \boldsymbol{V}_{ps}\left(\beta_2\right)\right) \tag{11f}$$

where (as mentioned above) scaling is solved once the relationships for the fields are obtained.
Three velocity fields are provided in Eqs (11) but there can be only one and therefore for a consistent velocity expression it is necessary that $R_1 = R_1^{\rho} = R_1^{v} = R_1^{u}$; achieved by setting identical the functions α_1^{ρ}, α_1^{v} and α_1^{u}. Any additional fields of interest can be easily derived from Eqs. (11) and for convenience the fields of interest in this paper are presented in Table 2.

Table 2: General zeroth-order and first-order finite similitude relationships

Properties	Zeroth-order identities	First-order identities
Density	$\rho_{ps} = \alpha_{01}^{\rho}\rho_{ts1}\beta_1^3$	$\rho_{ps} = \alpha_{01}^{\rho}\rho_{ts1}\beta_1^3 + R_1\left(\alpha_{01}^{\rho}\rho_{ts1}\beta_1^3 - \alpha_{02}^{\rho}\rho_{ts2}\beta_2^3\right)$
Displacement	$\boldsymbol{u}_{ps} = \beta_1^{-1}\boldsymbol{u}_{ts1}$	$\boldsymbol{u}_{ps} = \beta_1^{-1}\boldsymbol{u}_{ts1} + R_1\left(\beta_1^{-1}\boldsymbol{u}_{ts1} - \beta_2^{-1}\boldsymbol{u}_{ts2}\right)$
Velocity	$\boldsymbol{v}_{ps} = g_1\beta_1^{-1}\boldsymbol{v}_{ts1}$	$\boldsymbol{v}_{ps} = g_1\beta_1^{-1}\boldsymbol{v}_{ts1} + R_1(g_1\beta_1^{-1}\boldsymbol{v}_{ts1} - g_2\beta_2^{-1}\boldsymbol{v}_{ts2})$
Acceleration	$\boldsymbol{a}_{ps} = g_1^2\beta_1^{-1}\boldsymbol{a}_{ts1}$	$\boldsymbol{a}_{ps} = g_1^2\beta_1^{-1}\boldsymbol{a}_{ts1} + R_1(g_1^2\beta_1^{-1}\boldsymbol{a}_{ts1} - g_2^2\beta_2^{-1}\boldsymbol{a}_{ts2})$
Stress	$\boldsymbol{\sigma}_{ps} = \alpha_{01}^{\rho}g_1^2\beta_1\boldsymbol{\sigma}_{ts1}$	$\boldsymbol{\sigma}_{ps} = \alpha_{01}^{\rho}g_1^2\beta_1\boldsymbol{\sigma}_{ts1} + R_1\left(\alpha_{01}^{\rho}g_1^2\beta_1\boldsymbol{\sigma}_{ts1} - \alpha_{02}^{\rho}g_2^2\beta_2\boldsymbol{\sigma}_{ts2}\right)$
Strain	$\boldsymbol{\varepsilon}_{ps} = \boldsymbol{\varepsilon}_{ts1}$	$\boldsymbol{\varepsilon}_{ps} = \boldsymbol{\varepsilon}_{ts1} + R_1\left(\boldsymbol{\varepsilon}_{ts1} - \boldsymbol{\varepsilon}_{ts2}\right)$
Force	$\boldsymbol{F}_{ps} = \alpha_{01}^{\rho}g_1^2\beta_1^{-1}\boldsymbol{F}_{ts1}$	$\boldsymbol{F}_{ps} = \alpha_{01}^{\rho}g_1^2\beta_1^{-1}\boldsymbol{F}_{ts1} + R_1(\alpha_{01}^{\rho}g_1^2\beta_1^{-1}\boldsymbol{F}_{ts1} - \alpha_{02}^{\rho}g_2^2\beta_2^{-1}\boldsymbol{F}_{ts2})$
Moment	$\boldsymbol{M}_{ps} = \alpha_{01}^{\rho}g_1^2\beta_1^{-2}\boldsymbol{M}_{ts1}$	$\boldsymbol{M}_{ps} = \alpha_{01}^{\rho}g_1^2\beta_1^{-2}\boldsymbol{M}_{ts1} + R_1(\alpha_{01}^{\rho}g_1^2\beta_1^{-2}\boldsymbol{M}_{ts1} - \alpha_{02}^{\rho}g_2^2\beta_2^{-2}\boldsymbol{M}_{ts2})$

The field relationships in Table 2 are exact, but it is recognized that errors are very much a feature of experimental studies. Although this is the topic of future work the similitude identities however do provide some insight into the effect of errors and to illustrate this consider for example the displacement identity $\boldsymbol{u}_{ps} = \beta_1^{-1}\boldsymbol{u}_{ts1} + R_1\left(\beta_1^{-1}\boldsymbol{u}_{ts1} - \beta_2^{-1}\boldsymbol{u}_{ts2}\right)$. The reality of scaled experimentation is errors $\boldsymbol{\delta}_{ts1}^{u}$ and $\boldsymbol{\delta}_{ts2}^{u}$ in the trial-space field displacements $\boldsymbol{u}_{ts1}$ and $\boldsymbol{u}_{ts2}$, respectively, which on substitution returns the identity $\boldsymbol{\delta}_{ps}^{u} = \beta_1^{-1}\boldsymbol{\delta}_{ts1}^{u} + R_1\left(\beta_1^{-1}\boldsymbol{\delta}_{ts1}^{u} - \beta_2^{-1}\boldsymbol{\delta}_{ts2}^{u}\right)$, where $\boldsymbol{\delta}_{ps}^{u}$ is the error in $\boldsymbol{u}_{ps}$. Although the actual error in the physical space depends very much on the problem and how close the virtual model replicates the physical behaviour, this error equation nevertheless provides insight into the required accuracy needed in the trial spaces to achieve acceptable outcomes in the physical space.

4. SCALING OF STRUCTURAL ELEMENTS

This focus in this section is on the scaled behaviour of basic structural elements such as columns, beams, and struts under static loads. The purpose here is twofold, firstly to provide a gentle introduction into the application of the similitude theory and, secondly, to understand better the response of more complex structures through insights gleaned from an appreciation about the behaviour of basic structural elements under scaling. The relatively simple case studies examined in this section are analysed both analytically and numerically with the aid of the finite element package ABAQUS [31].

4.1. Scaling of Beam-Strut Model

Beams are important structural components that can withstand loads primarily by resisting bending and serve to transfer loads to walls, girders, and adjacent compression members. An appreciation of how beams scale is important for scaled experiments and to that end consider a simple setup of an I-section steel beam connected to a circular hollow steel strut. The arrangement examined is depicted in Fig. 1, where shown are both the full and scaled models, which have been recreated in the Abaqus finite element software and each are subjected to a concentrated force at the free end.

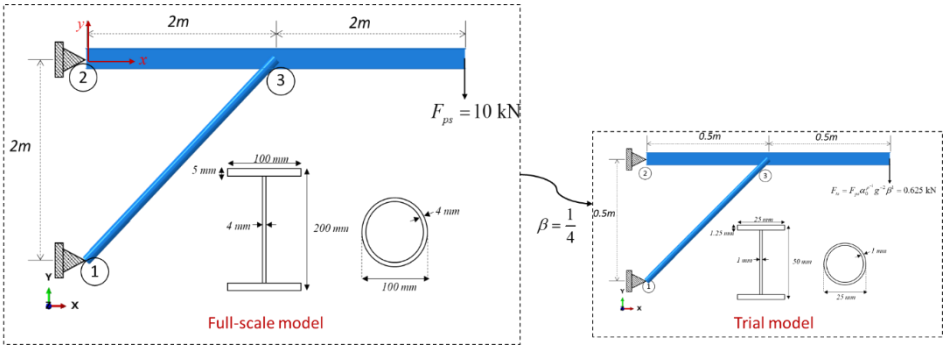

Figure 1. Full-scale and trial model of the beam-strut model

The models in Abaqus are meshed with identical numbers of elements of type B31, which is a 2-noded linear beam element and identical materials are used for both the trial-space and full-scale models. To verify the types of analysis, an initial comparison was performed between analytical and numerical models. This provided end deflections of 22.425mm and 22.419mm for the respective analytical and numerical models, so providing high confidence in the modelling approach.

Shear force and bending moment are described by the respective expressions,

$$V_{ps}(x_{ps}) = \begin{cases} -F_{ps} & 0 < x_{ps} < 2 \\ F_{ps} & 2 < x_{ps} < 4 \end{cases} \tag{12a}$$

$$M_{ps}(x_{ps}) = \begin{cases} -F_{ps}x_{ps} & 0 < x_{ps} < 2 \\ F_{ps}x_{ps} & 2 < x_{ps} < 4 \end{cases} \tag{12b}$$

and examination of Table 2 provides the zeroth-order scaling identities $V_{ps} = \alpha_0^{\rho} g^2 \beta^{-1} V_{ts}$ and $M_{ps} = \alpha_0^{\rho} g^2 \beta^{-2} M_{ts}$. In a similar fashion the standard expression for normal stress, scales according to the zeroth-order relationship $\sigma_{ps} = \alpha_{01}^{\rho} g_1^2 \beta_1 \sigma_{ts1}$ in Table 2 since

$$\sigma_{ps} = \frac{M_{ps} y_{ps}}{I_{ps}} = \frac{\alpha_0^{\rho} g^2 \beta^{-2} M_{ts} \beta^{-1} y_{ts}}{\beta^{-4} I_{ts}} = \alpha_0^{\rho} g^2 \beta \frac{M_{ts} y_{ts}}{I_{ts}} = \alpha_0^{\rho} g^2 \beta \sigma_{ts} \tag{13}$$

where I_{ps} and I_{ts} are second moments of area, y_{ps} and y_{ts} the distances measured from the neutral axes of the beams in their respective spaces.

Note that the similitude relationships provide the means to communicate the behaviour of the trial model to the physical space. They in effect provide the projected-trial model identified in Table 3, where maximum bending moments, reaction forces at the supports, and end displacements both analytically and numerically obtained, are tabulated. Note that the projected-trial models provide an almost perfect match for both analytical and numerical models when compared with the full-space results. A slightly greater mismatch is observed on a direct comparison of analytically and numerically obtained results. Even at this early stage, the benefit offered by scaling is being revealed with high levels of conformity.

Table 3: Detailed comparison of full-scale and projected trial model for beam-strut model

		Analytical			Numerical (FEM)		
		Trial Model	Projected Trial Model	Full-scale Model	Trial Model	Projected Trial Model	Full-scale Model
End Displacement (mm)		5.6065	22.4260	22.425	5.6047	22.4191	22.4190
Reaction force (kN)	Rx @1	1.25	20	20	1.25	20	19.999
	Ry @1	1.25	20	20	1.202	19.232	19.250
	Rx @2	1.25	20	20	1.25	20	19.999
	Ry @2	0.625	20	10	0.576	9.226	9.228
Maximum Moment (MNmm)		0.3125	20	20	0.313	20.320	20.271
Maximum Stress (N/mm^2)		169.5682	169.5682	169.5682	171.865	171.865	171.865

4.2. Scaling of a Steel Column Exposed to Buckling

Examined in this section are the phenomena of linear buckling and post-buckling of an important structural element, i.e., the I-section column. The buckling phenomenon might be anticipated to provide a challenge for scaled experimentation since initial imperfections can influence the outcome. Understanding the scaled behaviour of buckling for columns and beams under axial compression load is of interest as flexural and torsional stability problems can result. A detailed analytical and numerical examination into the buckling of an I-section aluminium-alloy column is provided in reference [32]. Flexural buckling is reasonably well captured by the simple relationship,

$$P_{cr} = \frac{\pi^2 EI}{L_{eff}^2} \tag{14}$$

where P_{cr} is the critical buckling load, E is Young's modulus of the material, I is the cross-sectional second moment of area, and L_{eff} is the effective length, which is dictated by column boundary conditions.

Prior to the investigation of the scaled effects on scaled columns, the proposed I-section column model is verified analytically and numerically in accordance with the study presented in reference [32]. The details of the full and scaled models are provided in Fig. 2. Initial verification results for critical-buckling loads are tabulated in Table 4 for both analytical and numerical predictions and contrasted with those of reference [30]. The closeness of the predictions provides good confidence in the proposed models. The simply supported column (6m in length) is made of aluminium alloy 5083 with material properties: Youngs modulus $E = 67600$ MPa, Poisson ratio $\nu = 0.33$, and yield stress $\sigma_y = 159.1$ MPa. The stress-strain behaviour of the aluminium alloy is described by the Ramberg-Osgood relationship [33],

$$\varepsilon = \frac{\sigma}{E} + K\left(\frac{\sigma}{\sigma_y}\right)^{n-1} \tag{15}$$

where the material constants $K = 0.002$ and $n = 8.8202$ [34].

The analytical solution is verified with the Abaqus finite element software package and to obtain the critical buckling load, a linear buckling analysis is performed initially. The model makes use of shell elements of type S4R with reduced integration, which are a 4-noded doubly curved, thin element and the mesh consists of a total of 46800 nodes. After linear-buckling analysis, post-buckling analysis is performed to observe the behaviour of the column on applying nonlinear material properties (i.e., Eq. (15)). The Ramberg-Osgood law is applied in Abaqus with deformational plasticity by the specification of two parameters, which are yield offset $\alpha = K E/\sigma_y$ and the hardening exponent $n-1$ [35].

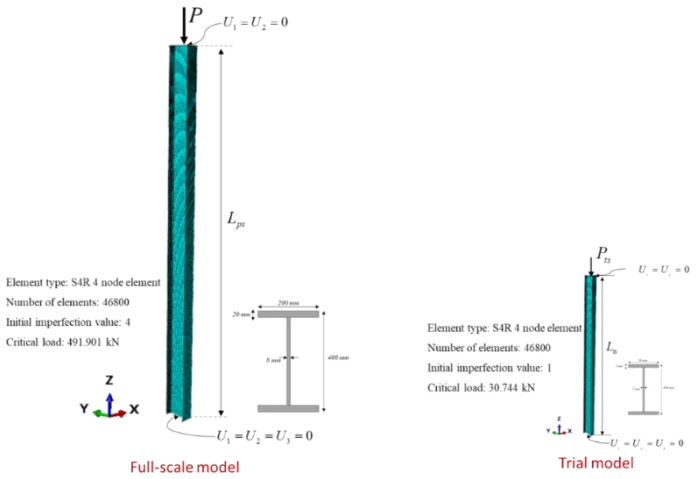

Figure 2. Finite element model with applied load and boundary conditions and cross-section of the full-scale and trial model

Table 4: Critical buckling load of a simply supported I-section column.

	Current Analysis		Szymczak and Kujawa [30]	
	Analytical	Numerical	Analytical	Numerical
Linear-buckling load (kN)	494.496	491.901	494.5	491.2

The main instability analysis is performed in Abaqus using the Static-RIKS command, which is a variation on the classical arc-length method for defining an initial geometric imperfection. The global imperfection amplitude is set to $L/1500$ (L is column length), which generally provides promising results when compared to experimental tests [36][37]. With this setup, the model is now primed for investigation of the load-deflection under scaling.

4.2.1. Scaling of flexural column buckling

The *finite similitude* theory is applied to the models depicted in Fig. 2 with a length scaling factor of $\beta = \frac{1}{4}$ and by means of the *zeroth-order theory* (i.e., identity Eq. (5)) the structure under scaling is investigated. The material of the column is the same for both scaled and full-scale models with scaling parameters obtained via the scaling rules (see Table 2). An initial comparison is made for linear buckling analysis for the full-scale and trial model as shown in Fig. 3.

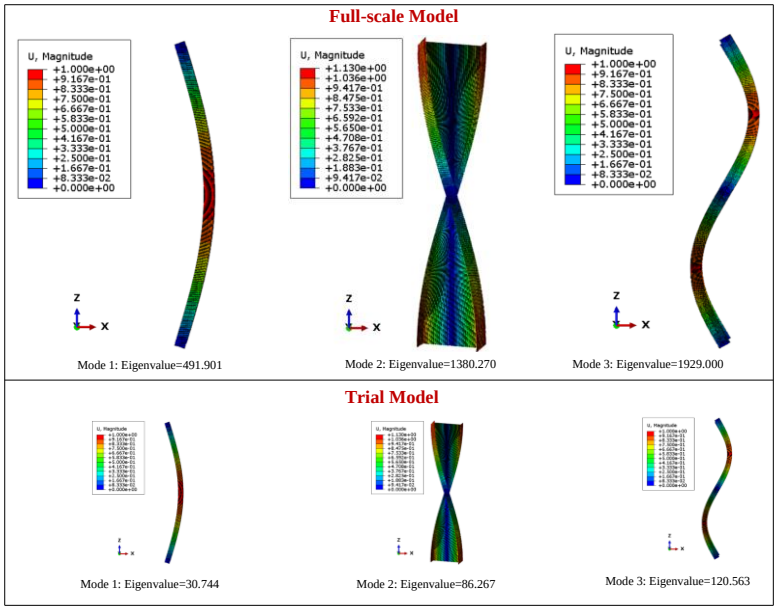

Figure 3. Comparison between linear buckling eigenmodes and eigenvalues (critical buckling load) of full-scale and trial model

The critical load obtained from linear buckling analysis is in exact agreement for both the full-scale and trial-scale models, where the full-scale critical load equates to β^{-2} times that of trial-space model. This is anticipated from Eq. (14), since Table 2 provides the stress and strain relationships $\boldsymbol{\sigma}_{ps} = \alpha_{01}^{\rho} g^2 \beta \boldsymbol{\sigma}_{ts}$ and $\boldsymbol{\varepsilon}_{ps} = \boldsymbol{\varepsilon}_{ts1}$, and consequently $E_{ps} = \alpha_0^{\rho} g^2 \beta E_{ts}$, which on substitution into Eq. (15) gives,

$$\left(P_{cr}\right)_{ps} = \frac{\pi^2 E_{ps} I_{ps}}{\left(L_{eff}\right)_{ps}^2} = \frac{\pi^2 \left(\alpha_0^{\rho} g^2 \beta E_{ts}\right)\left(\beta^{-4} I_{ts}\right)}{\beta^{-2}\left(L_{eff}\right)_{ts}^2} = \left(\alpha_0^{\rho} g^2 \beta\right)\beta^{-2} \frac{\pi^2 E_{ts} I_{ts}}{\left(L_{eff}\right)_{ts}^2} = \alpha_0^{\rho} g^2 \beta^{-1}\left(P_{cr}\right)_{ts} \tag{16}$$

which is in accordance with force relationship $\boldsymbol{F}_{ps} = \alpha_0^{\rho} g^2 \beta^{-1} \boldsymbol{F}_{ts}$ (see Table 2) but since $E_{ps} = E_{ts}$ it follows that $\alpha_0^{\rho} g^2 \beta = 1$ and consequently $\left(P_{cr}\right)_{ps} = \beta^{-2}\left(P_{cr}\right)_{ts}$.

The outcome of the post-buckling, nonlinear-stability analysis is provided in Fig. 4, where the projected trial-space results are contrasted against the full-scale predictions. Perfect agreement is achieved for the load-deflection response of the column, providing further evidence of the efficacy of the zeroth-order theory in this case.

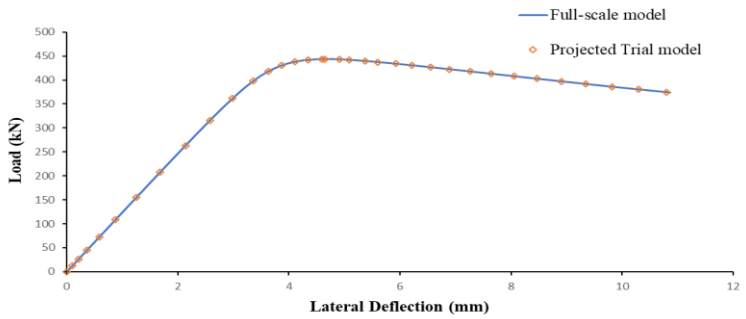

Figure 4. Load–lateral displacement curves for comparison

4.3. The Thin-section Problem

The relatively simple examples considered thus far satisfy Eq. (4) and the rules of zeroth-order finite similitude. It is of interest at this stage to maintain the relative simplicity but introduce a problem that fails to satisfy Eq. (4) yet conforms to identity Eq. (6a), i.e., *first-order finite similitude*. An important area of active research for scaled experimentation is around the concept of geometric similarity as defined by dimensional analysis. It can be desirable on practical grounds to break the rules of geometric similarity especially if thin structural elements are involved, where one or more of the structural dimensions are significantly smaller than the others. For pronounced scaling ratios that are often needed when scaling large structures (e.g., bridges, skyscrapers) the limitation imposed by thinner sections can be particularly constraining. Unrepresentative behaviour such as localized buckling and tearing can be the product of very thin sections along with standard of-the-shelf items being unavailable. The open literature in this area is underpinned by dimensional analysis and is case dependent involving ad-hoc practical fixes and consequently does not provide a systematic unified solution [38–42]. It is of interest therefore to assess whether first-order finite similitude can provide any insight into this problem for structural elements. The scaling of a cantilever beam under a concentrated load is again examined but, in this case, geometric similarity is broken in some manner. Detailed in Fig. 5 is a rectangular hollow box section cantilever beam possessing the critical feature of interest, i.e., a thin wall.

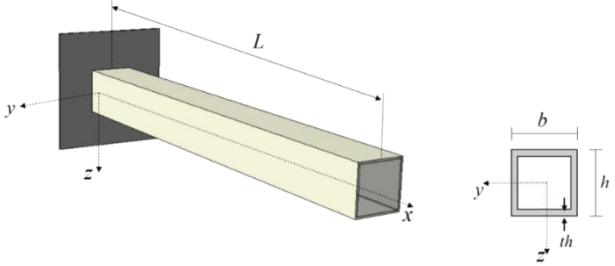

Figure 5. Rectangular hollow cross-section cantilever beam and cross-section

The detailed geometries are presented in Table 5 for full-scale, trial-1, and trial-2 models. The scaling factors for two trial-space models are set to $\beta_1 = \frac{1}{5}$ and $\beta_2 = \frac{1}{10}$ but imposed on the experimental designs is the constraint that the wall thickness *th* is greater or equal to 1mm (i.e., $th \geq 1\text{mm}$). Note from Table 5 that the geometric dimensions *h* (height), *b* (width) and *L* (length) are all scaled according to the geometric scaling rule, i.e., they scale with β . The thickness however is constrained and therefore does not obey this rule and, in both trial-space models it is set to the minimum required thickness of 1 mm.

Table 5: Material properties and geometric dimensions of box-section beams

	Variables	Full-scale	Trial-1 model	Trial-2 model
	b (mm)	50	10	5
	h (mm)	50	10	5
	th (mm)	4	1	1
	L (mm)	1000	200	100
	Density (ton/mm^3 x10^{-9})	7.85	7.85	7.85
	Young's modulus (GPa)	210	210	210
	Yield stress (MPa)	355	355	355
	Poisson ratio	0.3	0.3	0.3

Case Study 1	Applied Force (N)	2000	80	20
	Measured tip displacement (mm)	12.14	2.065	0.7
Case Study 2	Applied Force (N)	4500	215	82.5

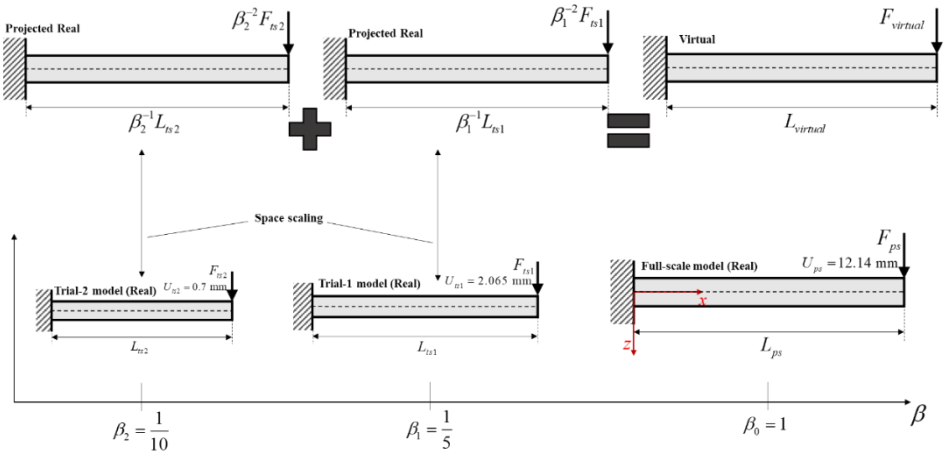

Figure 6. Physical space and Projected trial models for the cantilever beam

Shown in Fig. 6 is a schematic of the first order approach applied to the box-section beam involving two scaled experiments that are projected onto the physical space and combined to provide a virtual model that attempts to capture the behaviour of the full-scale system. The use identical of materials throughout reduces the relationships $\alpha_{01}^{\rho} g_1^2 \beta_1 E_{ts1} = E_{ps}$ and $\alpha_{02}^{\rho} g_2^2 \beta_2 E_{ts1} = E_{ps}$ to $\alpha_{01}^{\rho} g_1^2 = \beta_1^{-1}$ and $\alpha_{02}^{\rho} g_2^2 = \beta_2^{-1}$ respectively, which simplifies the force and stress relationships in Table 2 to

$$F_{ps} = \beta_1^{-2} F_{ts1} + R_1 (\beta_1^{-2} F_{ts1} - \beta_2^{-2} F_{ts2}) \tag{17a}$$

$$\sigma_{ps} = \sigma_{ts1} + R_1 (\sigma_{ts1} - \sigma_{ts2}) \tag{17b}$$

where R_1 is the parameter defined by Eq. (10) that is required to be set, where the lateral beam deflection is,

$$U_{ps} = \beta_1^{-1} U_{ts1} + R_1 \left(\beta_1^{-1} U_{ts1} - \beta_2^{-1} U_{ts2} \right) \tag{17c}$$

Two case studies are considered with case study 1 limited to linear behaviour described by analytical relationships and case study 2 examining the nonlinear response but analysed numerically. The steel material used in the study is defined to behave as an elastic, perfectly plastic material. The loading conditions for both case studies are detailed in Tab. 5. Consider then the linear response of the cantilever, and since β_1, β_2 and F_{ps} are known, a convenient approach for the determination of R_1 is to firstly assume zeroth-order relationships for force and set $F_{ts1} = \beta_1^2 F_{ps}$ and $F_{ts2} = \beta_2^2 F_{ps}$, which ensures Eq. (17a) is satisfied. Secondly, the free-end tip displacements for each beam provided by the analytical relationships where $U_{ts1}^{max} = \dfrac{F_{ts1} L_{ts1}^3}{3 E_{ts1} I_{ts1}}$ and $U_{ts2}^{max} = \dfrac{F_{ts2} L_{ts2}^3}{3 E_{ts2} I_{ts2}}$ can be substituted into Eq. (17c) to give the value of R_1 to be,

$$R_1 = \frac{U_{ps}^{max} - \beta_1^{-1} U_{ts1}^{max}}{\beta_1^{-1} U_{ts1}^{max} - \beta_2^{-1} U_{ts2}^{max}} \tag{18}$$

which provides a simple procedure for the determination of R_1 in this case, which in this case provides $R_1 = 0.5465$.

The tip displacement for the full-scale and virtual model is calculated (with $R_1 = 0.5465$) and not too unexpectedly an exact match in this case, since R_1 is set to ensure this outcome. With R_1 determined, Eq. (17c) can now be employed to provide a prediction for the beam displacement shown in Fig. 7(a), which perfectly replicates the behaviour of the full-scale beam. Similarly, Eq. (17b) provides the means to examine normal stress, the results of which are presented in Fig. 7. Note that normal stress at the outer fibres of the beam is in perfect agreement between the virtual and full-scale models as indicated in Fig. 7(b). However, this is not the full story since there is a deviation in the vicinity of the upper and lower walls of the virtual and full-scale beams. The normal stress is plotted along the mid-span of the two beams in Fig. 7(c). The reason for the difference is

connected to the breakage of geometric similarity, which resulted in the two projected models in Fig. 6 having different outer-wall thicknesses and satisfying the inequalities $th < \beta_1^{-1} th_{ts1} < \beta_2^{-1} th_{ts2}$. This means that stress values exist in the virtual model that is not present in the full-scale model as illustrated in Fig. 7(c). The issue is of little real concern, however since the important field information recovered from the virtual is that which overlaps with the full-scale model and for this example at least full replication is achieved.

To examine the nonlinear response of the beam (case study 2) the commercial software package Abaqus is applied, with the beam represented with 2-noded linear beam elements (B31). The first order scaling parameter R_1 is obtained using Eq. (17a) using the forces detailed in Tab. 5, which returns a value $R_1 = 0.304$. Eq. (17c) is then applied to calculate the beam displacement of the first order virtual model, which is contrasted against the full-scale model as presented in Fig. 8(a), where an exact match is revealed. The reason for the exact prediction is shown in Fig. 8(b), where Eq. (7b) provides for perfect replication of the nonlinear stress-strain behaviour.

The study in this section demonstrates that first-order finite similitude can return an exact representation for a situation where the traditional definition of similarity does not hold. Although a relatively simple example and the focus of future work (with and without buckling), it nevertheless demonstrates two important features, i.e., an exact new form of similitude exists and breaking geometric similarity to a certain degree is possible and potentially very useful.

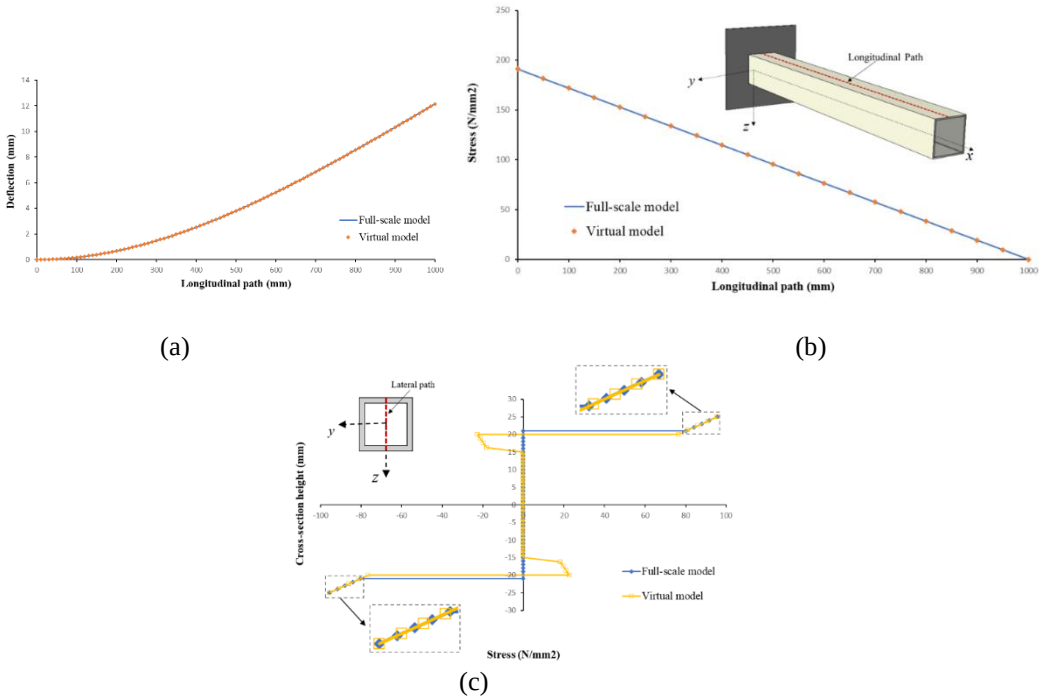

Figure 7. Global and local behaviour of the stress field (a) Beam deflection for the proposed design (b) Longitudinal distribution of the maximum normal stress (@z=h/2), (c) Lateral distribution of the normal stress at mid-span.

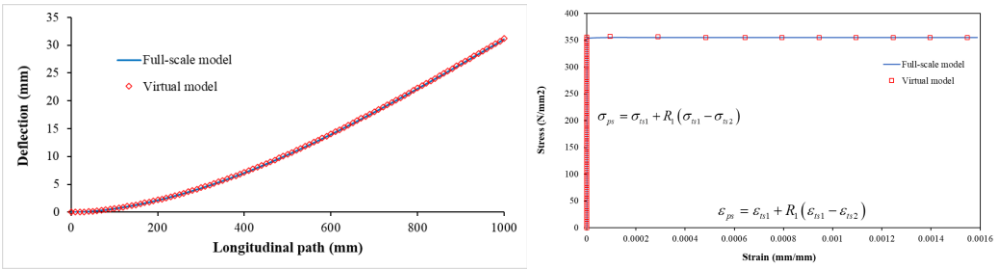

Figure 8. Nonlinear response of a cantilever beam subjected to an end load (a) Beam deflection along the length of the beam (b) Stress-strain curve at the clamped end.

5. SCALING OF AN EIGHT-STORY LONG-SPAN STEEL BUILDING

This section focuses on the application of zeroth and first-order finite similitude to the earthquake loading of a high-rise, long-span building structure. This type of building is selected as the case study to focus the analysis on how the finite-similitude theory can be applied in seismic scenarios. It is recognized as mentioned above that pronounced scaling factors can give rise to significant scale effects arising from mass and gravity. The traditional "solution" to this problem is additional mass [14] or incrementation of the base acceleration. The case study here is designed to examine this problem to ascertain whether the new theory can provide a possible solution. Added-mass approaches are invariably breaking geometric similarity and increases in acceleration limit the materials that can be employed and can rule out the use of identical materials. Acceleration can be shown to be inversely proportional to the dimension scaling factor β, so it can take on impractically high values for buildings such as high rises.

In order to provide realism in the study, the Chi-Chi Earthquake, which yields very high dynamic earth pressures, is applied as the time-acceleration ground motion (depicted in Fig. 9 (a) [43]). All beams and columns in all eight stories are identical (with the same cross-sectional area, length) and slabs in all eight stories. The building has a span of 7.2 m on each side with a floor height of 3.2 m and the slab thickness is assumed to be of 100 mm and the beams and columns are modelled with I sections (IPE450) and box profiles (Box 500×500×30), respectively [44].

The whole structure and all components are modelled in the Abaqus finite element software as depicted in Fig. 9 (b), where the B31 linear beam element (i.e., a first-order, three-dimensional beam element) is utilized to simulate the columns and beams. The use of this element significantly reduces the number of degrees of freedom involved providing a convenient platform for repeat calculations. The slab is meshed with S4R elements (i.e., four-node shell elements) with each node having six degrees of freedom.

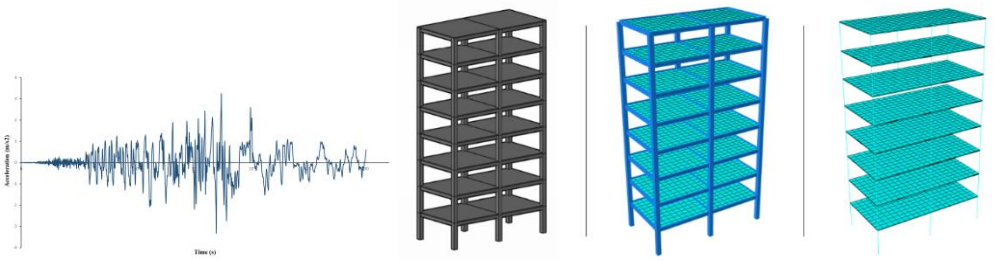

(a) (b)

Figure 9. (a) Acceleration – Time graph for Chi-Chi earthquake **(b)** The eight-story building CAD model and finite element meshed parts

Another important consideration when modelling steel or reinforced concrete structures is critical damping. Abaqus has several methods for the dissipation of energy in dynamic systems with the specification of damping sources. Four different damping sources exist in Abaqus; these are: material and damping system; damping with time integration; modal damping; and global damping. In the case of earthquake phenomena best practice for implicit and explicit methods is Rayleigh damping [45,46] with the critical viscous damping factor for this analysis is set to 5% [47–50]. The scaled models are designed according to the similarity laws with identical materials used for both full-scale and trial models to test out their ability to capture the effects of earthquake loading on a full-scale building structure. The dimension scales selected for the study are $\beta_1 = \frac{1}{10}$ and $\beta_2 = \frac{1}{20}$, and both zeroth and first-order theories are applied with details presented in Table 6.

Table 6: Material properties for physical, trial 1 and trial 2 models

Properties	Physical Model	Trial 1 Model	Trial 2 Model
Material (Steel)	S355	S355	S355
Density (kg/m^3)	7850	7850	7850
Young's modulus (GN/m^2)	210	210	210
Yield stress (MN/m^2)	3.55	3.55	3.55
Damping ratio (ξ)	5%	5%	5%
Gravity (m/s^2)	9.807	9.807	9.807
Acceleration (m/s^2)	1	1	1
Scaling factors	$\beta_0 = 1$	$\beta_1 = 1/10$	$\beta_2 = 1/20$
Time (s)	$g_0 = 1$	$g_1 = 1/10$	$g_2 = 1/20$
Additional mass (kg)		No add. mass	No add. mass

The aim here is to adopt identical materials for both full-scale and trial models and consequently the zeroth order relationships for density ($\rho_{ps} = \alpha_{01}^{\rho}\rho_{ts1}\beta_1^3$) and Young's modulus ($E_{ps} = \alpha_{01}^{\rho} g_1^2 \beta_1 E_{ts1}$) reduce to $\rho_{ps} = \rho_{ts1}$ and $E_{ps} = E_{ts1}$ with $\alpha_{01}^{\rho} = \beta_1^{-3}$ and $g_1 = \beta_1$. This latter condition provides the zeroth-order acceleration relationship $\boldsymbol{a}_{ts1} = \beta_1^{-1}\boldsymbol{a}_{ps}$ (see Table 2), which confirms that as $\beta_1 \to 0$ the acceleration applied to the scaled model increases as $\beta_1^{-1} \to \infty$. It is appreciated that increasing the acceleration can return promising results but there is patently a limit to what is practicable. Staying within a reasonable range for acceleration for pronounced scaling factors excludes both dimensional analysis and zeroth-order finite similitude.

It is of interest to examine the scope of *first-order finite similitude*, which combines the information from two scaled experiments, to deal with this issue. The first-order acceleration relationship $\boldsymbol{a}_{ps} = g_1^2\beta_1^{-1}\boldsymbol{a}_{ts1} + R_1(g_1^2\beta_1^{-1}\boldsymbol{a}_{ts1} - g_2^2\beta_2^{-1}\boldsymbol{a}_{ts2})$ (see Table 2) is the focus here in view of the limitations mentioned above. Recall that each trial model is restricted to designs utilising the same material and zeroth-order considerations provide the relationships $\alpha_{01}^{\rho} = \beta_1^{-3}$ & $\alpha_{02}^{\rho} = \beta_2^{-3}$ and $g_1 = \beta_1$ & $g_2 = \beta_2$. Observe that these latter two conditions mean that the first-order relationship for acceleration reduces to $\boldsymbol{a}_{ps} = \beta_1\boldsymbol{a}_{ts1} + R_1(\beta_1\boldsymbol{a}_{ts1} - \beta_2\boldsymbol{a}_{ts2})$. The ground acceleration (as shown in Fig. 9 (a)) is assumed to act in one direction with identical accelerations applied in all models, i.e., $a_{ps} = a_{ts1} = a_{ts2}$, and additionally it is an evident requirement is that gravitational accelerations are equal, i.e., $G_{ps} = G_{ts1} = G_{ts2}$. These constraints imposed on the equation $\boldsymbol{a}_{ps} = \beta_1\boldsymbol{a}_{ts1} + R_1(\beta_1\boldsymbol{a}_{ts1} - \beta_2\boldsymbol{a}_{ts2})$ provide $R_1 = \frac{1-\beta_1}{\beta_1-\beta_2} = 18$.

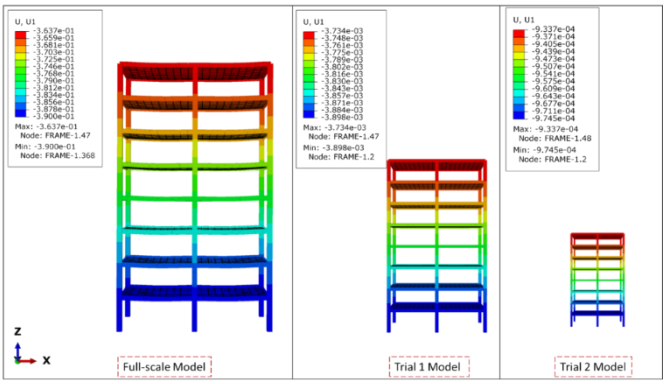

Figure 10. Numerical deformed shapes of the physical and scaled models

The full-scale and both trial models are simulated by the Abaqus finite element software (details above) and the results obtained are presented in Fig. 11. The roof displacement and the story drift of the physical model and the first-order virtual model are presented using the first-order displacement relationship in Tab. 2.

The results obtained illustrate the vast promise and the benefits of two scaled experiments over a single experiment. This example demonstrates the ability of the finite similitude theory to evaluate the behaviour of structures with information gleaned from two experiments. The result in Fig. 11 (a) shows that the extracted results are orders of magnitude more accurate than those obtainable from a single experiment. It also worth emphasising that no recourse to additional mass or other acceleration increments is needed and the way this is achieved is not by changing the problem but by changing the similitude condition.

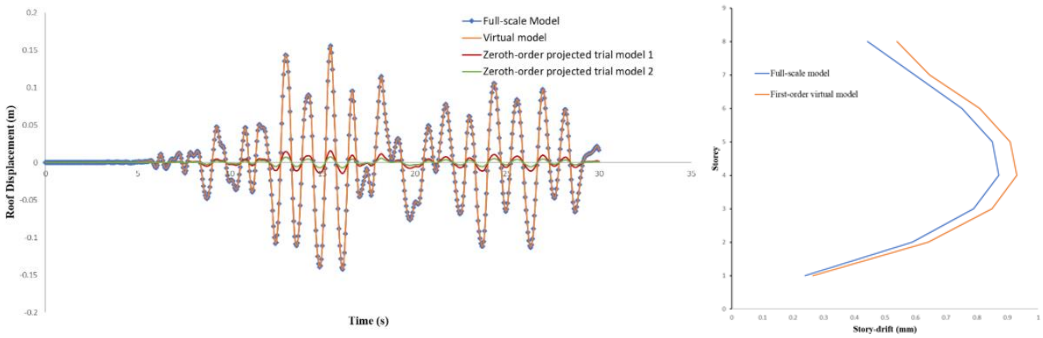

(a) (b)

Figure 11. (a) Comparison of the top displacement of the full-scale model, first-order and zeroth-order virtual models **(b)** Story drift analysis of the full-scale and virtual models

Additionally, to examine the nonlinear dynamic response of the eight story long-span building depicted in Fig. 9 (b), it is subjected a gradually increasing cyclic dynamic loading as detailed in Fig. 12(a). Nonlinear analysis is performed on each of the trial models, and the results of these are combined in accordance with the first-order theory and presented in Fig. 12(b). Examination of this figure reveals a high level of agreement with the full-scale model confirming once again the efficacy of the first order similitude condition. All the models in this study are made of identical material with properties tabulated in Table 6 and $R_1 = 18$ as in the earthquake loading case.

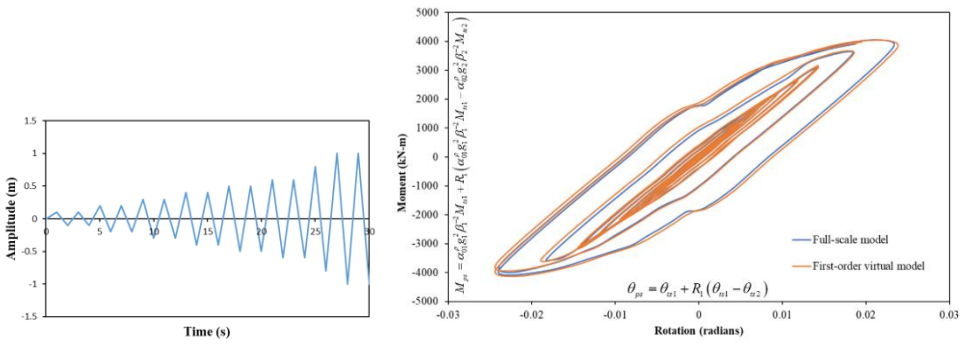

(a) (b)

Figure 12. (a) Applied cyclic loading scheme (b) moment-rotation response of the full-scale and virtual models

6. SEISMIC PERFORMANCE OF A STEEL BUILDING EQUIPPED WITH NONLINEAR FLUID VISCOUS DAMPERS

Additional sophistication is incorporated into the building design investigated in this section with the inclusion of dampers in the structure. The steel construction frame examined involves eight stories and six bays in each direction, where the area plan is 36m x 36m, and the elevation view of the structure is detailed in Fig. 13 with column and beam sections [51] identified. The detailed section properties of the beams and columns are listed in Table 7. The steel used for all structural elements in full-scale and scaled-down models is ST37 steel grade. In addition, to perform a nonlinear time history analysis, the commercial finite element Sap2000 software package [52] is used and the Northridge (1994) acceleration-time (see Fig. 14 (a)) data is applied in the x-direction of the building as a ground motion. The structural damping is estimated to be at 5% and the placement of the fluid viscous dampers (FVDs) and the building details are in accordance with reference [51].

Table 7: Cross-sections of the beams and columns[51]

Structure	Story	C1	C2	B1	B2
8-story steel frame	1	RHS 360 × 20	RHS 550 × 30	W 18 × 46	W 21 × 111
	2	RHS 240 × 20	RHS 500 × 30	W 18 × 46	W 21 × 111
	3	RHS 200 × 20	RHS 450 × 25	W 18 × 46	W 21 × 111
	4	RHS 180 × 18	RHS 450 × 25	W 18 × 46	W 21 × 111
	5	RHS 180 × 18	RHS 400 × 20	W 18 × 46	W 21 × 93
	6	RHS 180 × 18	RHS 400 × 20	W 18 × 46	W 21 × 73
	7	RHS 180 × 18	RHS 360 × 20	W 18 × 46	W 21 × 50
	8	RHS 180 × 18	RHS 300 × 20	W 18 × 40	W 21 × 44
Slab (Shell)	All	100 mm thickness			

It is widely recognised that one of the most effective devices to dissipate energy during the action of an earthquake is a fluid viscous damper [53]. The details of the fluid viscous damper used in this study are provided by Mehdi et al. [51]. The main parameters of the viscous dampers are the damping coefficient, velocity exponent α and the lateral stiffness provided by the supporting bar, which in that case are 2942.5 kNs/m, 0.5 and 39004 kN/m respectively.

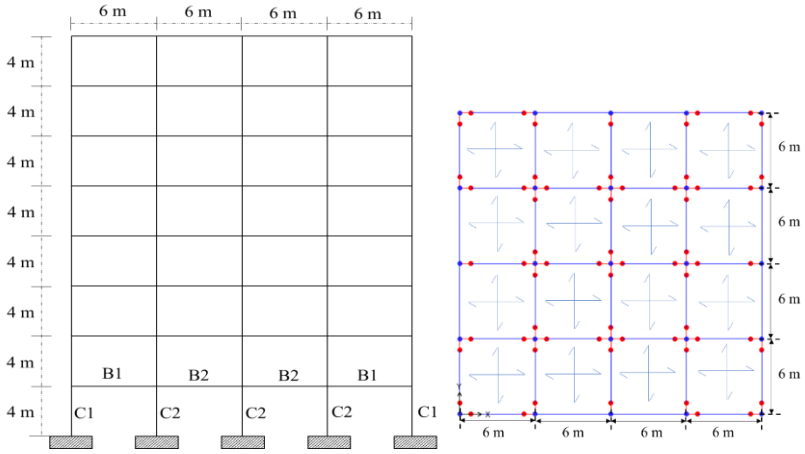

Figure 13. Elevation view and the plan grid layout of the model

The fluid viscous damper is defined as a link property in Sap2000 and the fluid damper is constrained to act only along the axial direction of the damper and thus constrained in directions that are perpendicular to its axis. Fig. 14 (b) shows the 2D elevation view of the structure along with the placements of the FVDs.

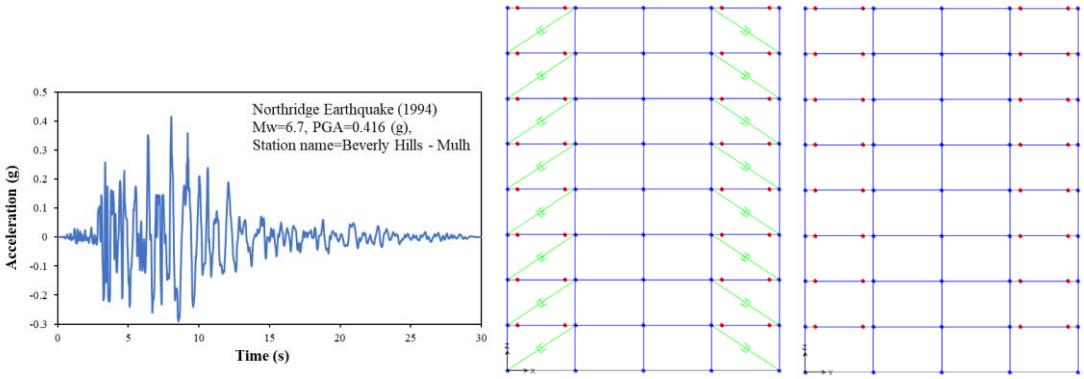

(a) (b)

Figure 14. (a) Applied Northridge earthquake record **(b)** Sap2000 elevation view of the model with FVDs

Based on a mesh-sensitivity study (see Tab. 8), the minimum numbers of elements for the beams and columns to guarantee convergence of the numerical solution, capturing the behaviour of the structure are 320 and 200, respectively; this mesh is applied in the presented case study.

Table 8: Mesh sensitivity analysis results

Column elements	Beam elements	Total number of elements	Max. top displacement (m)
200	320	520	0.3705
1000	1600	2600	0.3706
4000	6400	10400	0.3706
8000	12800	20800	0.3699

With the full-scale model now defined, the geometric scaling parameters are set for trial models 1 and 2, which are $\beta_1 = \frac{1}{6}$ and $\beta_2 = \frac{1}{10}$, respectively. These scaling factors should be selected carefully according to laboratory capacities and equipment limitations. As a preliminary investigation a controlled displacement pushover analysis is performed prior to full dynamic analysis of the proposed building. Such an analysis provides an opportunity to observe nonlinear behaviour under quasistatic loading. This is facilitated by the application of hinge properties applied automatically to the ends of the beams to observe how localised plastic behaviour translates to an overall nonlinear response. The nonlinear static pushover analysis is conducted on both trial models and a moment-rotation graphs are produced and presented in Fig. 16 (b), where perfect agreement, between full scale and individual scaled models is revealed.

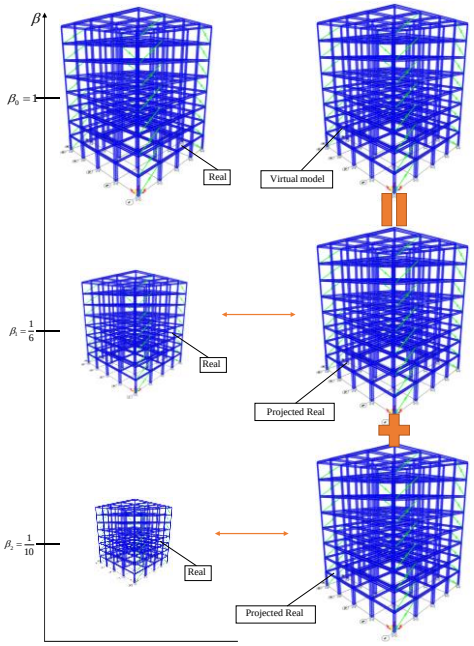

Figure 15. Full-scale and scaled models of the 8-story steel building

For dynamic analysis, it is not possible to capture the buildings behaviour using a single scaled model due to the added complexity involved, necessitating the need for additional scaling degrees of freedom. In this case, the scaled models are analysed using the same software (i.e., Sap2000) to observe their behaviour to predict the full-scale model behaviour under earthquake loading. The configuration of the three models is presented in Fig. 15 along with corresponding projected models. Given that identical materials are used throughout the scaling parameters related to density and time are set to $\alpha_{01}^{\rho} = \beta_1^{-3}$ & $\alpha_{02}^{\rho} = \beta_2^{-3}$ and $g_1 = \beta_1$ & $g_2 = \beta_2$. The boundary and loading conditions are defined as in the previous case study, where gravitational acceleration and applied acceleration is equal for the three models, which as above, returns $R_1 = 12.5$ from the relationship $R_1 = \frac{1-\beta_1}{\beta_1 - \beta_2}$

The damping coefficients for structural damping and the FVDs follow different scaling rules as described in reference [54]. The Rayleigh damping coefficients for structural damping obeys the relationship $c_{ps} = \beta^{-2} c_{ts}$, which can be contrasted with the damping coefficients for the FVDs, which satisfy the relationship $c_{ps} = \beta^{-\alpha} c_{ts}$, where this latter condition assumes no change in the damping fluid used. Note, however, it is possible to achieve the identity $c_{ps} = \beta^{-2} c_{ts}$ for the FVDs with a change in damping fluid. This is a practical change but it does require that the damping fluid has an appropriate viscosity [55,56]. Both these options are explored here.

Fig. 16 (a) and 17(a) present the behaviour of the full-scale model and the virtual model with the damping coefficients for the FVDs behaving as $c_{ps} = \beta^{-\alpha} c_{ts}$ and $c_{ps} = \beta^{-2} c_{ts}$, respectively. It is clear on examination of Fig. 16 (a) that there is a significant difference between the virtual and full-scale results with a mismatch in oscillation frequency. In comparison to the prediction in Fig. 16 (a), Fig. 17 (a) highlights the benefits of changing the silicone oil in the scaled FDVs. In this case the behaviour of the FVDs follows the same scaling behaviour as structural damping and the outcome is a small overall error. The results demonstrate promising agreement with the full-scale model outputs and indicate the benefit of careful material selection. Further evidence of the high level of agreement between the models is found in Figs. 17 (b), (c) and 18 with results for story displacement & inter-story drift ratios, and the base shear force, respectively. Overall, the results obtained from the first-order finite similitude theory provide confidence in the efficacy of the approach for predicting the behaviour of tall buildings.

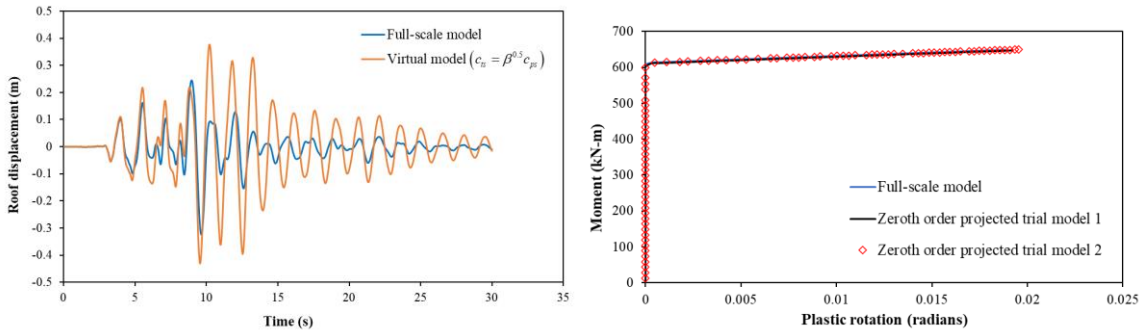

(a) (b)

Figure 16. (a) Roof displacement comparison between full-scale and virtual models with the same silicone oil in the trial nonlinear FVDs, (b) Moment-rotation comparison of full-scale and zeroth-order projected trial models.

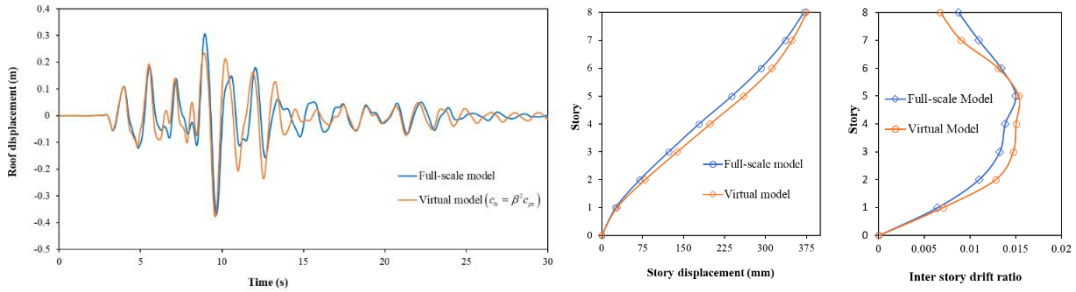

(a) (b) (c)

Figure 17. (a) Roof displacement comparison of the full-scale and virtual model with alternative silicone oil in the trial nonlinear FVDs **(b)** Story displacement and **(c)** inter-story drift ratio comparison for full-scale and virtual models

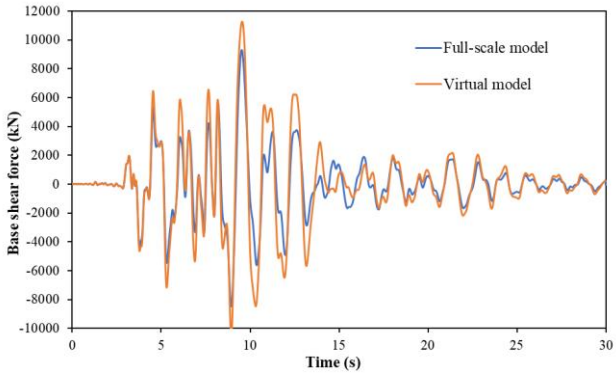

Figure 18. Base shear force comparison of the full-scale and virtual models

CONCLUSION

The paper focused on the application of the finite-similitude theory by means of an initial examination of structural elements through to the analysis of whole-building structures under earthquake excitation. Two trial models at distinct scales were combined to predict full-scale behaviour in situations where classical dimensional analysis failed. The efficacy of this approach was demonstrated with a high level of accuracy returned in the results and no requirement for additional mass or base accelerations to be artificially raised. The following conclusions can be drawn from the specific trials involving both analytical and numerical analysis:

1. The robustness and efficacy of a new form of similitude involving two scaled experiments have been reaffirmed through analytical and numerical studies applied to basic and practical structural engineering case studies.
2. It has been demonstrated how the first-order finite similitude rule provides an approach that enables identical ground accelerations (and gravitational) to be applied to full and scaled models. This was achieved without recourse to material substitutions and extraordinary experimental setups (e.g., use of centrifuge systems or additional mass techniques). This was demonstrated for an eight-story steel building case study where the two-experiment approach returned predictions of full-scale behaviour with

no error (i.e., 0% error) contrasted against a like-for-like single-experimental result (i.e., no additional mass, same material) of 90% error.

3. The first-order finite similitude rule has been confirmed to provide accurate predictions for a high-rise building containing non-linear viscous dampers, although a degree of physical modelling was required, i.e., the substitution of damping oil in the scaled dampers. The case study demonstrated that the combination of two trial models could replicate the physical behaviour of the full-scale model with accuracy for roof displacement and maximum story displacement.
4. The first-order finite similitude rule has been shown to be able to break the rule of geometric similarity as traditionally defined. This was demonstrated for a thin-walled beam, where the theory successfully captured the exact global behaviour of the full-scale model for displacement and stress, despite the wall thickness not following geometric scaling.
5. Nonlinear material responses were captured exactly in the thin-sectioned cantilever beam and in the pushover analysis for an 8-story steel building. No consideration was given to ductile responses arising from concrete cracking at this stage but there exists no barrier to their inclusion given the generic nature of the proposed scaling approach.

ACKNOWLEDGEMENTS

The authors would like to acknowledge The Ministry of National Education in Turkey and the Department of Civil Engineering at Firat University for providing support for Muhammed Atar to facilitate his doctoral research at the University of Manchester.

REFERENCES

[1] Sedov LI, Friedman M, Holt M, Cole JD. Similarity and Dimensional Methods in Mechanics. J Appl Mech 1961. https://doi.org/10.1115/1.3640458.

[2] Buckingham E. On physically similar systems; Illustrations of the use of dimensional equations. Phys Rev 1914;4:345–76. https://doi.org/10.1103/PhysRev.4.345.

[3] Kline SJ, Radbill JR. Similitude and Approximation Theory. J Appl Mech 1966;33:238–238. https://doi.org/10.1115/1.3625015.

[4] Buckingham E. The principle of similitude . Nature 1915;96:396–7. https://doi.org/10.1038/096396d0.

[5] Sharma A, Reddy GR, Vaze KK. Shake table tests on a non-seismically detailed RC frame structure. Struct Eng Mech 2012;41:1–24. https://doi.org/10.12989/sem.2012.41.1.001.

[6] Nayak S, Dutta SC. Failure of masonry structures in earthquake: A few simple cost effective techniques as possible solutions. Eng Struct 2016;106:53–67. https://doi.org/10.1016/j.engstruct.2015.10.014.

[7] Guerrero H, Ji T, Escobar JA, Teran-Gilmore A. Effects of Buckling-Restrained Braces on reinforced concrete precast models subjected to shaking table excitation. Eng Struct 2018;163:294–310. https://doi.org/10.1016/j.engstruct.2018.02.055.

[8] Garevski M, Hristovski V, Talaganov, Kosta; Stojmanovska M. Experimental Investigations of 1/3-Scale R/C Frame with Infill Walls Building Structures. Proc. 13th World Conf. Earthq. Eng., 2004, p. 772.

[9] Kim SE, Lee DH, Ngo-Huu C. Shaking table tests of a two-story unbraced steel frame. J Constr Steel Res 2007;63:412–21. https://doi.org/10.1016/j.jcsr.2006.04.009.

[10] Petry S, Beyer K. Scaling unreinforced masonry for reduced-scale seismic testing. Bull Earthq Eng 2014;12:2557–81. https://doi.org/10.1007/s10518-014-9605-1.

[11] Zou Y, Lu XL. Shaking table model test on Shanghai World Financial Center. World Inf Earthq Eng 2007.

[12] Mohammed A, Hughes TG, Mustapha A. The effect of scale on the structural behaviour of masonry under compression. Constr Build Mater 2011;25:303–7. https://doi.org/10.1016/j.conbuildmat.2010.06.025.

[13] Knappett JA, Reid C, Kinmond S, O'Reilly K. Small-scale modeling of reinforced concrete structural elements for use in a geotechnical centrifuge. J Struct Eng 2011;137:1263–71. https://doi.org/10.1061/(ASCE)ST.1943-541X.0000371.

[14] Li S, Zuo Z, Zhai C, Xu S, Xie L. Shaking table test on the collapse process of a three-story reinforced concrete frame structure. Eng Struct 2016;118:156–66. https://doi.org/10.1016/j.engstruct.2016.03.032.

[15] Bairrao R, Vaz C. Shaking table testing of civil engineering structures-The LNEC 3D simulator experience. 2th World Conf Earthq Eng 2000;2129.

[16] Carrillo J, Gonzalez G, Llano L. Evaluation of mass-rig systems for shaking table experiments. DYNA 2012;79:159–67.

[17] Saiidi MS, Douglas B. Shake Table Testing of Flexure Dominated Reinforced Concrete Bridge Columns Report No . CCEER 99-13 Patrick Laplace Center for Earthquake Engineering Research. 1999.

[18] Chen X, Guan Z, Li J, Spencer BF. Shake Table Tests of Tall-Pier Bridges to Evaluate Seismic Performance. J Bridg Eng 2018;23. https://doi.org/10.1061/(ASCE)BE.1943-5592.0001264.

[19] Moghaddam M, Darvizeh R, Davey K, Darvizeh A. Scaling of the powder compaction process. Int J Solids Struct 2018;144–145:192–212. https://doi.org/10.1016/j.ijsolstr.2018.05.002.

[20] Sadeghi H, Davey K, Darvizeh R, Darvizeh A. A scaled framework for strain rate sensitive structures subjected to high rate impact loading. Int J Impact Eng 2019;125:229–45. https://doi.org/10.1016/j.ijimpeng.2018.11.008.

[21] Al-Tamimi A, Darvizeh R, Davey K. Experimental investigation into finite similitude for metal forming processes. J Mater Process Technol 2018;262:622–37. https://doi.org/10.1016/j.jmatprotec.2018.07.028.

[22] Ochoa-Cabrero R, Alonso-Rasgado T, Davey K. Scaling in biomechanical experimentation: A finite similitude approach. J R Soc Interface 2018. https://doi.org/10.1098/rsif.2018.0254.

[23] Sadeghi H, Davey K, Darvizeh R, Darvizeh A. Scaled models for failure under impact loading. Int J Impact Eng 2019;129:36–56. https://doi.org/10.1016/j.ijimpeng.2019.02.010.

[24] Davey K, Darvizeh R, Al-Tamimi A. Scaled metal forming experiments: A transport equation approach. Int J Solids Struct 2017;125:184–205. https://doi.org/10.1016/j.ijsolstr.2017.07.006.

[25] Davey K, Sadeghi H, Darvizeh R, Golbaf A, Darvizeh A. A Finite Similitude Approach to Scaled Impact Mechanics. Int J Impact Eng 2021;148. https://doi.org/10.1016/j.ijimpeng.2020.103744.

[26] Davey K, Darvizeh R, Atar M, Golbaf A. A Study of Scale Effects in Discrete Scaled Dynamic Systems. Int J Mech Sci 2021.

[27] Darvizeh R, Davey K. A transport approach for analysis of shock waves in cellular materials. Int J Impact Eng 2015;82:59–73. https://doi.org/10.1016/j.ijimpeng.2014.11.006.

[28] Darvizeh R, Davey K. Non-physical finite element method: Multiple material discontinuities. Comput Struct 2016;164:145–60. https://doi.org/10.1016/j.compstruc.2015.11.010.
[29] Darvizeh R, Davey K. Non-physical finite element modelling of high speed normal crushing of cellular materials. Int J Impact Eng 2015;82:130–43. https://doi.org/10.1016/j.ijimpeng.2015.04.002.
[30] Davey K, Darvizeh R. Neglected transport equations: extended Rankine–Hugoniot conditions and J -integrals for fracture. Contin Mech Thermodyn 2016;28:1525–52. https://doi.org/10.1007/s00161-016-0493-2.
[31] Abaqus U manual. Version 6.14. Dassault Systèmes Simulia Corp, Provid RI 2014.
[32] Szymczak C, Kujawa M. Flexural buckling and post-buckling of columns made of aluminium alloy. Eur J Mech A/Solids 2019;73:420–9. https://doi.org/10.1016/j.euromechsol.2018.10.006.
[33] Ramberg W, Osgood WR. Description of stress-strain curves by three parameters. Natl Advis Comm Aeronaut 1943.
[34] Szymczak C, Kujawa M. Local buckling of thin-walled channel member flange made of aluminum alloy. AIP Conf. Proc., 2017. https://doi.org/10.1063/1.4977688.
[35] Hibbett, Karlsson, Sorensen. ABAQUS/standard: User's Manual. 1998.
[36] Theofanous M, Gardner L. Testing and numerical modelling of lean duplex stainless steel hollow section columns. Eng Struct 2009;31:3047–58. https://doi.org/10.1016/j.engstruct.2009.08.004.
[37] Ahmed S, Ashraf M. Numerical investigation on buckling resistance of stainless steel hollow members. J Constr Steel Res 2017;136:193–203. https://doi.org/10.1016/j.jcsr.2017.05.017.
[38] Kasivitamnuay J, Singhatanadgid P. Scaling laws for displacement of elastic beam by energy method. Int J Mech Sci 2017;128–129:361–7. https://doi.org/10.1016/j.ijmecsci.2017.05.001.
[39] Alves M, Oshiro RE. Scaling the impact of a mass on a structure. Int J Impact Eng 2006;32:1158–73. https://doi.org/10.1016/j.ijimpeng.2004.09.009.
[40] Oshiro RE, Alves M. Predicting the behaviour of structures under impact loads using geometrically distorted scaled models. J Mech Phys Solids 2012;60:1330–49. https://doi.org/10.1016/j.jmps.2012.03.005.
[41] Davey K, Darvizeh R, Golbaf A, Sadeghi H. The breaking of geometric similarity. Int J Mech Sci 2020;187:105925. https://doi.org/10.1016/j.ijmecsci.2020.105925.
[42] Luo Z, Zhu Y, Zhao X, Wang D. Determining Dynamic Scaling Laws of Geometrically Distorted Scaled Models of a Cantilever Plate. J Eng Mech 2016;142:04015108. https://doi.org/10.1061/(asce)em.1943-7889.0001028.
[43] Wu W, Ge S, Yuan Y, Ding W, Anastasopoulos I. Seismic response of subway station in soft soil: Shaking table testing versus numerical analysis. Tunn Undergr Sp Technol n.d.;100:103389. https://doi.org/10.1016/j.tust.2020.103389.
[44] Rahnavard R, Fard FFZ, Hosseini A, Suleiman M. Nonlinear analysis on progressive collapse of tall steel composite buildings. Case Stud Constr Mater 2018;8:359–79. https://doi.org/10.1016/j.cscm.2018.03.001.
[45] Song Z, Su C. Computation of Rayleigh Damping Coefficients for the Seismic Analysis of a Hydro-Powerhouse. Shock Vib 2017;2017:1–11. https://doi.org/10.1155/2017/2046345.
[46] Chen XM, Duan J, Qi H, Li YG. Rayleigh Damping in Abaqus/Explicit Dynamic Analysis. Appl Mech Mater n.d.;627:288–94. https://doi.org/10.4028/www.scientific.net/amm.627.288.
[47] Cremer L, Heckl M. Structure-Borne Sound. 1988. https://doi.org/10.1007/978-3-662-10121-6.
[48] Vince Adams and Abraham Askenazi. Building Better Products with Finite Element Analysis. vol. 127. New York: American Society of Mechanical Engineers; n.d.
[49] Bachmann H, Ammann WJ, Deischl F, Eisenmann J, Floegl I, Hirsch GH, et al. Vibration Problems in Structures. 1995. https://doi.org/10.1007/978-3-0348-9231-5.
[50] Orban F. Damping of materials and members in structures. J Phys Conf Ser 2011;268. https://doi.org/10.1088/1742-6596/268/1/012022.
[51] Banazadeh M, Ghanbari A, Ghanbari R. Seismic performance assessment of steel moment-resisting frames equipped with linear and nonlinear fluid viscous dampers with the same damping ratio. J Constr Steel Res 2017;136:215–28. https://doi.org/10.1016/j.jcsr.2017.05.022.
[52] CSI. SAP2000. Analysis Reference Manual. CSI Berkeley (CA, USA) Comput Struct INC 2016.
[53] Ras A, Boumechra N. Seismic energy dissipation study of linear fluid viscous dampers in steel structure design. Alexandria Eng J 2016;55:1–12. https://doi.org/10.1016/j.aej.2016.07.012.
[54] Davey K, Darvizeh R, Atar M, Golbaf A. A Study of Scale Effects in Discrete Scaled Dynamic Systems. Int J Mech Sci 2021;199:106399. https://doi.org/10.1016/j.ijmecsci.2021.106399.
[55] Boksmati JI, Madabhushi GSP. Centrifuge modelling of structures with oil dampers under seismic loading. Earthq Eng Struct Dyn 2020;49:356–74. https://doi.org/10.1002/eqe.3243.
[56] Huneault J, Kamil J, Higgins A, Plant D. Dynamic tensile strength of silicone oils. AIP Conf. Proc., 2018. https://doi.org/10.1063/1.5044825.

APPENDIX

Nomenclature

E_{ps}	Young modulus of the physical space
E_{ts}	Young modulus of the trial space
F_{ps}	Force of physical space
F_{ts}	Force of the trial space
g	Time scaling factor
I_{ps}	Second moment of area of physical space
I_{ts}	Second moment of area of trial space
n	Ramberg-Osgood material constant
K	Ramberg-Osgood material constant
σ	Stress field
σ_y	Yield stress
P_{cr}	Linear buckling critical load
R_1	First-order scaling parameter
U_{ps}	Displacement of the physical space
U_{ts1}	Displacement of the trial space 1
U_{ts2}	Displacement of the trial space 2
L_{ts1}	Length of the cantilever beam in trial space 1
L_{ts2}	Length of the cantilever beam in trial space 2
α	Fluid viscous damper velocity exponent
c	Damping coefficient
v_{ts}^{*}	Control volume velocity of trial space
v_{ps}^{*}	Control volume velocity of physical space
v_{ps}	Velocity of the physical space
v_{ts}	Velocity of the trial space
α_0^{ψ}	Scalar for transport equation for field ψ
ψ	Physical field
$\alpha_0^{\psi} T_0^{\psi}$	Scaled transport equation for field ψ
α^{ρ}	Density scaling factor
α^{v}	Momentum scaling factor
α^{u}	Movement scaling factor
α^{1}	Volume scaling factor
$\boldsymbol{a}_{ts}$	Acceleration of physical space
$\boldsymbol{a}_{ts}$	Acceleration of trial space

G	Gravitational acceleration
β	Length scalar
Γ	Control volume Ω boundary
ε_{ts}	Strain of trial space
ε_{ps}	Strain of physical space
ν	Poisson ratio
ρ_{ps}	Density of physical space
ρ_{ts}	Density of trial space
χ	Arbitrary coordinate in the reference space
ψ	Physical field
Ω	Control volume
Ω_{ps}	Control volume over the physical space
Ω_{ts}	Control volume over trial space
Ω^{*}_{ps}	Reference space for the control volume
Ω^{*}_{ts}	Reference space for the control volume
Ω^{*ref}_{ts}	Reference control volume in trial space